GEOSPHERE

GEOSPHERE; v. 16, no. 2

https://doi.org/10.1130/GES02149.1

11 figures; 5 tables; 1 set of supplemental files

CORRESPONDENCE: ioannidi@gfz-potsdam.de

CITATION: Ioannidi, P.I., Angiboust, S., Oncken, O., Agard, P., Glodny, J., and Sudo, M., 2020, Deformation along the roof of a fossil subduction interface in the transition zone below seismogenic coupling: The Austroalpine case and new insights from the Malenco Massif (Central Alps): Geosphere, v. 16, no. 2, p. 510–532, https://doi.org/10.1130/GES02149.1.

Science Editor: Shanaka de Silva
Guest Associate Editor: Gray E. Bebout

Received 8 April 2019
Revision received 20 September 2019
Accepted 23 December 2019

Published online 13 February 2020

Deformation along the roof of a fossil subduction interface in the transition zone below seismogenic coupling: The Austroalpine case and new insights from the Malenco Massif (Central Alps)

Paraskevi Io Ioannidi[1], Samuel Angiboust[1,2], Onno Oncken[1], Philippe Agard[3], Johannes Glodny[1], and Masafumi Sudo[4]

[1]GFZ German Research Centre for Geosciences, D-14473 Potsdam, Germany
[2]Université de Paris, Institut de Physique du Globe de Paris, Centre National de la Recherche Scientifique (CNRS), F-75005 Paris, France
[3]Institut des Sciences de la Terre de Paris (ISTeP)–Unité Mixte de Recherche (UMR) 7193, Sorbonne Université, F-75005 Paris, France
[4]Institut für Geowissenschaften, Universität Potsdam, 14476 Potsdam, Germany

ABSTRACT

A network of fossil subduction plate interfaces preserved in the Central Alps (Val Malenco, N Italy) is herein used as a proxy to study deformation processes related to subduction and subsequent underplating of continental slices (in particular the Margna and Sella nappes) at depths reported to in the former brittle-ductile transition. Field observations, microfabrics, and mapping revealed a network of shear zones comprising mostly mylonites and schists but also rare foliated cataclasites. These shear zones are either located at the contacts of the two nappes or within the boundaries of the Sella unit. Microprobe results point to two different white mica generations, with higher-pressure (Si-rich) phengites rimming lower-pressure (Si-poor) phengites. Garnet is locally observed overgrowing resorbed pre-Alpine cores. Pressure-temperature estimates based on pseudosection modeling point to peak burial deformation conditions of ~0.9 GPa and 350–400 °C, at ~30 km depth. Rb/Sr geochronology on marbles deformed during the Alpine event yields an age of 48.9 ± 0.9 Ma, whereas due to incomplete recrystallization, a wide range of both Rb/Sr and $^{40}Ar/^{39}Ar$ apparent ages is obtained from deformed orthogneisses and micaschists embracing 87–44 Ma.

Based on our pressure-temperature, structural and geochronological observations, the studied shear zones last equilibrated at depths downdip of the seismogenic zone in an active subduction zone setting. We integrate these new results in the frame of previous studies on other segments of the same Alpine paleosubduction interface, and we propose that this system of shear zones represents deformation conditions along the subduction interface(s) in the transition zone below the seismogenic zone during active subduction.

INTRODUCTION

Subduction zones commonly evidence strong interplate coupling and large magnitude earthquakes in the seismogenic zone (e.g., Hyndman et al., 1997; Conrad et al., 2004; Heuret and Lallemand, 2005). Investigating deformation processes taking place along and in the vicinity of their interface can shed light on properties such as the distribution of seismicity or the effective rheology along the interface (e.g., Stöckhert, 2002; Herrendörfer et al., 2015). Exhumed suture zones are important targets since they enable a direct insight on ancient subduction settings and provide opportunities to access the long-term record of subduction zone deformation (e.g., Ernst and Dal Piaz, 1978; Platt, 1986; Stöckhert, 2002; Agard et al., 2018). Metamorphic rocks from ancient sutures may yield information on how rock fabrics evolve with depth from shallow brittle seismogenic faults (Sibson, 2013; Yamaguchi et al., 2014; Saffer and Wallace, 2015) to deeper tremorgenic regions and beyond (Angiboust et al., 2015; Obara and Kato, 2016; Webber et al., 2018). While the shallow segments of the plate interface have been extensively documented thanks to a wealth of well-exposed key localities (Kitamura et al., 2005; Vannucchi et al., 2008; Bachmann et al., 2009b; Rowe et al., 2013), our understanding of deeper deformation processes (20–40 km depth) is hampered by the scarcity of direct observations on localities devoid of exhumation-related tectonic imprint. Even rarer is the natural record of deformation along the hanging wall of a subduction interface.

The European Central Alps represent a remarkable natural laboratory giving the opportunity to (nearly) continuously document hanging-wall processes from shallow levels exposed in Arosa and Engadine regions (Bachmann et al., 2009a, 2009b) down to deeper segments exposed in the Dent Blanche and Sesia complexes (Trümpy, 1975; Konrad-Schmolke et al., 2011; Angiboust et al., 2015; Jaeckel et al., 2018; Fig. 1). The subduction and accretion of continental slivers from the stretched Apulian margin over several millions of years against the Apulian buttress gave rise to the Austroalpine domain (Compagnoni et al., 1977; Dal Piaz et al., 2003). This composite nappe stack comprises individual slices separated by localized shear zones interpreted as transient slip interfaces and where local brittle and semi-brittle deformation patterns have been reported (Polino et al., 1990; Babist et al., 2006; Angiboust et al., 2014, 2015; Locatelli et al., 2018; Menant et al., 2018). While the Arosa-Engadine as well as Dent Blanche regions have been extensively investigated in the frame of the subduction interface model, the southern end of the Austroalpine complex in the

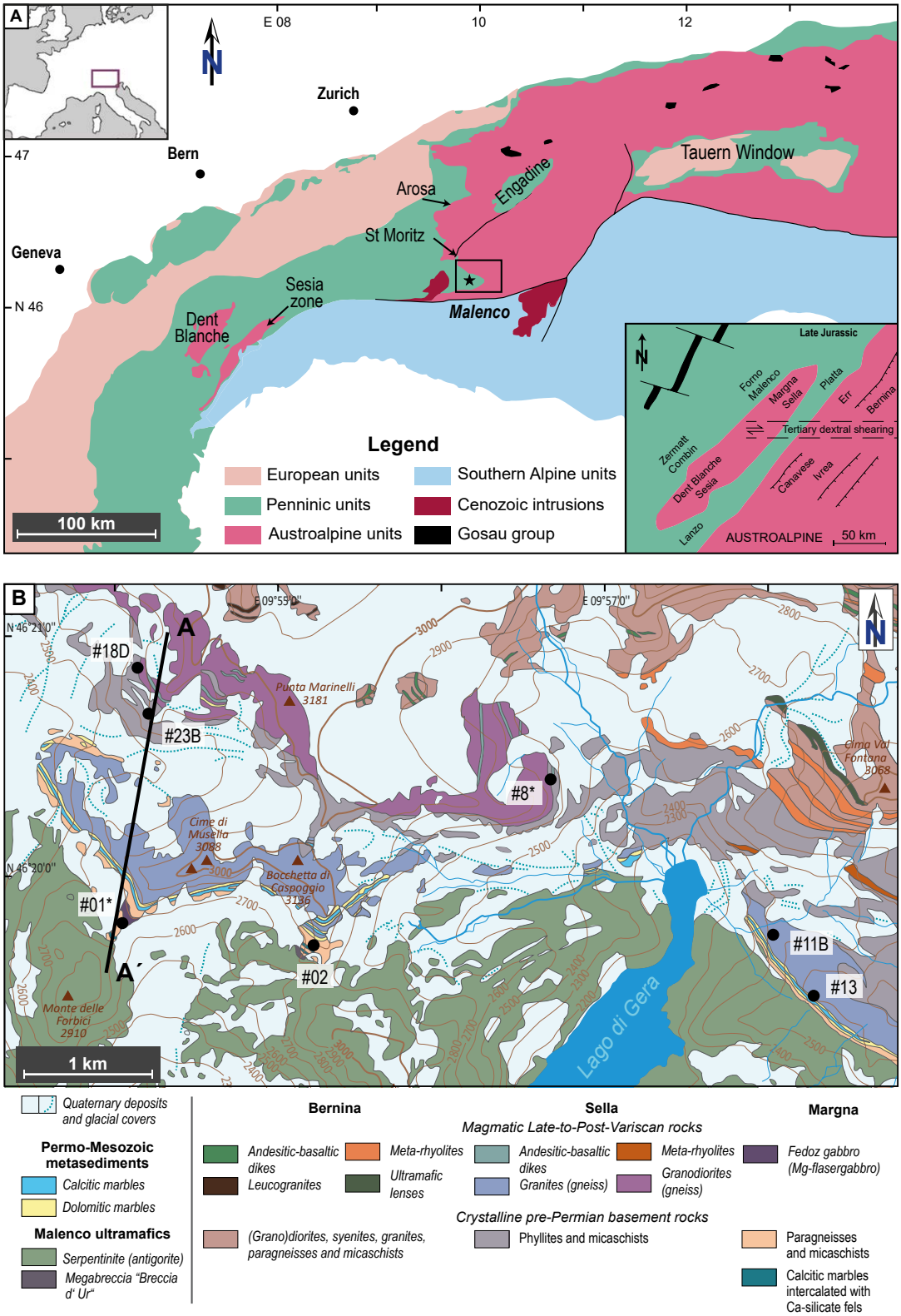

Figure 1. (A) Geological map of the Western and Central Alps showing the location of the Austroalpine nappes with respect to surrounding tectonic units. The studied area is located in the black box in the Val Malenco region. Inset: Paleogeographic reconstruction along the NW margin of the Apulian plate. Dent Blanche, Sesia, Margna, and Sella nappes are interpreted as extensional allochthons derived from the Apulian margin (modified from Froitzheim and Manatschal, 1996). (B) Geological map of the Val Malenco, modified from Montrasio et al. (2005). Shades of magenta colors represent units belonging to Sella nappe, beige to Margna nappe; also shown are the Malenco ultramafics (greenish) and the Bernina nappe (light brown). Black circles denote the sampling localities (e.g., #01* includes samples #01A, #01B, and #01F). For exact location, see also Table 1. Line A–A' shows the position of the cross section in Figure 2B.

Central Alps (Malenco region) remains unexplored despite its potential importance as the missing element linking the depths of the Arosa-Engadine (10–20 km) and Dent Blanche–Sesia massifs (40–60 km). We herein report field, pressure-temperature (P-T), and geochronological data from the aforementioned part of the Central Alps in order to study the processes taking place during subduction and underplating of the Margna and Sella nappes. We place particular emphasis on observing the deformation mechanisms in the plate interface zone(s) during subduction at the depth of the transition beneath the seismogenic zone as it is identified by instrumental observations to be below 350 °C and recently found to exhibit a diversity of slip behaviors (e.g., Obara and Kato, 2016, and references therein).

GEOLOGICAL SETTING

The Central Alps are the result of the convergence between the European and the Adriatic plates and their subsequent collision during Tertiary times (e.g., Ring et al., 1988; Liniger and Nievergelt, 1990; Handy, 1996; Schmid et al., 2004). Two distinct tectonic phases affected the region during the evolution of the Alpine edifice: east to southeast subduction of the Penninic units during the Cretaceous, which formed an oceanic domain between the two continental plates, accompanied by top-W thrusting and a later shift to N-S shortening with top-N directions in the Paleogene (e.g., Ratschbacher, 1986; Ring et al., 1988; Dürr, 1992; Handy, 1996).

The study area is located in Val Malenco, Central Alps, at the border of N Italy and SE Switzerland (Figs. 1A and 1B), precisely at the transition between the Austroalpine slice stack and the South Penninic oceanic domain. The major tectonic units in the study area are the Penninic Malenco-Forno unit, the overlying Austroalpine Margna and Sella nappes, both representing continental crust, and their sedimentary covers (e.g., Guntli and Liniger, 1989; Liniger and Nievergelt, 1990; Hermann and Müntener, 1992; Trommsdorff et al., 1993; Bissig and Hermann, 1999; Mohn et al., 2011).

Austroalpine Units and Their Permo-Mesozoic Sedimentary Covers

The continental Austroalpine units are represented in the study area by the Margna and the Sella nappes. Stratigraphic similarities between the Margna cover and sediments from the Lower Austroalpine Err nappe (Liniger and Guntli, 1988) suggest an Apulian affinity for the Margna nappe (Liniger, 1992). The Malenco and Platta nappes, which abut our studied units in the SW and NE, respectively, are former subcontinental mantle units exhumed during Jurassic rifting (Trommsdorff et al., 1993; Manatschal, 1995; Froitzheim and Manatschal, 1996). The position of Margna and Sella nappes between these two (ultra)mafic units reflects the primary complexity of the passive margin (Liniger, 1992; Spillmann, 1993). In this frame, Margna and Sella were extensional allochthons (e.g., Froitzheim and Manatschal, 1996), representing the transition from the Adria continental margin toward the South Penninic ocean basin during Jurassic, with Margna being the most distal part of the Adria continent (Hermann and Müntener, 1996; Hermann et al., 1997).

Both nappes encompass pre-Variscan continental rocks, mostly granodiorites and granites, which were later metamorphosed into orthogneisses (e.g., Staub, 1946; Liniger and Guntli, 1988; Guntli and Liniger, 1989; Hermann and Müntener, 1992). Occasionally, 2–3-m-thick andesitic and basaltic dikes crosscut the large igneous bodies for several hundreds of meters. A sequence of Mesozoic, mostly Cretaceous, sediments is covering the Margna and Sella basement rocks (Hermann and Müntener, 1992; Trommsdorff et al., 2005). The Margna nappe also contains an association of gabbros and lower crustal granulites (Hermann et al., 1997); this association is absent in Sella and is identical to the one found within the Malenco ultramafic units (Trommsdorff et al., 2005).

The boundaries between the Margna (lower) and the Sella (upper) units are marked by thin slices of sedimentary rocks (Figs. 2A and 2B; Hermann and Müntener, 1992). They comprise Triassic pre-rift marine shelf dolomite marbles and presumably Lower Jurassic syn-rift quartz-calcschists that locally contain dolomite breccias (Hermann and Müntener, 1992; Trommsdorff et al., 2005). Their formation is connected to the rifting phase of the Austroalpine units during Mesozoic times. Both sedimentary units exhibit Alpine metamorphism.

The Dent Blanche and Sesia units are considered equivalent to the Margna and Sella nappes in the Central Alps (Froitzheim and Manatschal, 1996; Froitzheim et al., 1996; Schmid et al., 2004). Both units consist of a polymetamorphic continental basement that was intruded by pre-Alpine granitoids and mafic bodies (e.g., Rubatto el al., 1999; Monjoie et al., 2007). Together, all four nappes (Margna, Sella, Dent Blanche, and Sesia) are thought to have represented extensional allochthons between two denuded mantle units, the Malenco to the west and the Platta to the east (e.g., Beltrando et al., 2010; inset of Fig. 1A).

Another Austroalpine unit in the broader Val Malenco area, not further studied here, however, is the Bernina nappe comprising intrusive rocks slightly deformed and with local Alpine metamorphic overprint (Fig. 1B; Rageth, 1984; Spillmann and Büchi, 1993; Trommsdorff et al., 2005).

Malenco-Forno Units

The Malenco unit, structurally beneath the Margna nappe (Figs. 2A and 2B), is mainly composed of ultramafic rocks (peridotite and spinel lherzolite) that are largely serpentinized and also retain ophicarbonates in various localities (Trommsdorff and Evans, 1977; Hermann and Müntener, 1992). A Jurassic crust-to-mantle transition is preserved near Mount Braccia, where gabbros and pelitic granulites are intermixed with the ultramafics as well as the Fedoz gabbro intrusion, also observed in the Margna unit (Gautschi, 1979, 1980; Ulrich and Borsien, 1996; Hermann et al., 1997). According to Trommsdorff et al. (1993) and Hermann et al. (1997), the Malenco ultramafics were a denudated subcontinental fragment of the Adriatic lithospheric plate later exhumed during Jurassic rifting. Subsequent exhumation of the unit to the ocean floor (Trommsdorff et al., 1993) is supported by serpentinization of the ultramafic units, rodingitization, and the formation of ophicarbonates (Müntener et al., 2000). During the Upper Cretaceous,

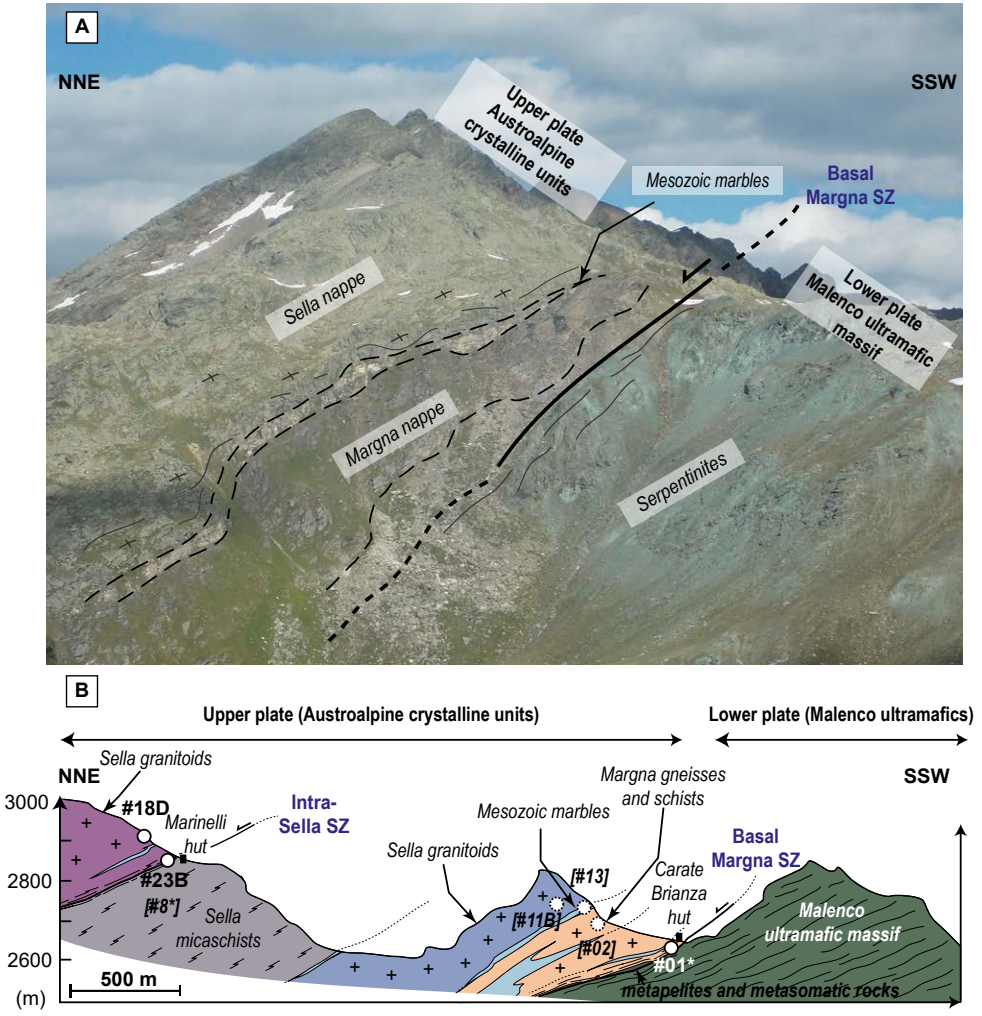

Figure 2. (A) Field picture showing the basal Margna shear zone (SZ) in the Pass d'Ur area; view from Rifugio Bignami. (B) Simplified cross section showing the structure of the studied area as well as sampling localities (#18 and #01). Star (*) refers to all three samples #01A, #01B, and #01F; samples in brackets and corresponding dotted circles denote localities that are not present in this cross section but in the equivalent units (see also map in Fig. 1B).

the Malenco ultramafics were overprinted by Alpine deformation and subsequently incorporated into the Alpine nappe stack (Müntener et al., 1997).

The Forno unit belongs tectonically to the same level as the Malenco unit and is a typical ocean floor sequence (Montrasio, 1973; Ferrario and Montrasio, 1976; Peretti, 1985) comprising volcaniclastic rocks and basalts. The whole oceanic crust sequence is overlain by middle Jurassic to late Cretaceous sediments (Peretti, 1985).

Alpine Metamorphic Ages in Val Malenco

The broader Val Malenco area and the three units that comprise it (Sella, Margna, and Malenco) have been the target of several petrological and structural studies focusing on the inherited, pre-Alpine structures and deformation observed in the nappes (e.g., Froitzheim and Manatschal, 1996; Hermann and Müntener, 1996; Bissig and Hermann, 1999; Müntener et al., 2000, 2010; Trommsdorff et al., 2005).

Only a few studies in the Val Malenco area have, so far, dealt with the timing of Alpine deformation and its imprint on older, preexisting structures (Fig. 3). Cretaceous greenschist-facies metamorphism in the southern Platta and Malenco units was initially recorded by Deutsch (1983), who obtained K-Ar amphibole ages spanning a range of 90–69 Ma. $^{40}Ar/^{39}Ar$ dating on riebeckite from Platta yielded apparent ages in the range of 89–70 Ma, while K-Ar dating on mica-bearing meta-radiolarites from the lower Austroalpine Err nappe yielded ages of 89–76 Ma for the first generation of white micas (parallel to S1 foliation; Handy et al., 1996) and 80–67 Ma for the second generation (parallel to S2; Handy et al., 1996). Finally, Villa et al. (2000) recognized two amphibole generations related to Alpine deformation from the Malenco ultramafics, one pressure and one temperature dominated, at 91–83 and 73–67 Ma, respectively. Mohn et al. (2011) suggest that deformation observed in the rocks of the Malenco ultramafics, as well as of S Platta, Margna, and Sella units, is possibly related to pressure-dominated metamorphism of P ~0.5–0.6 GPa (Bissig and Hermann, 1999). Despite relatively large uncertainties, Picazo et al. (2019) recently obtained ages of 63.0 ± 3.0 Ma for pressure metamorphism associated with nappe stacking and 54.7 ± 4.1 Ma for possibly peak temperature Alpine metamorphism.

The Subduction Interface through Time

Although the movement of the overriding plate has been systematically studied (Ratschbacher, 1986; Ring et al., 1988, 1989), and it was top-W during Cretaceous and top-N in Early Tertiary, the

exact location of the subduction interface in the study area has long been disputed. Southward to south-eastward subduction started in the South Penninic ocean between 120 and 100 Ma (Handy and Oberhänsli, 2004, and references therein) and, based on $^{40}Ar/^{39}Ar$ dating of pseudotachylytes from the base of the Austroalpine nappe stack, was active between 90 and 60 Ma (Bachmann et al., 2009b). Recently, high-pressure (HP) subduction-related metamorphism was reported by Droop and Chavrit (2014) for the Lanzada–Santa Anna metagabbros, a unit structurally beneath the Malenco ultramafics and south of our study area (black star in Fig. 1A). According to the authors, these eclogitic metagabbros corroborate the existence of a south-dipping subduction and place the interface beneath the Malenco unit, at some later stage during Alpine convergence history.

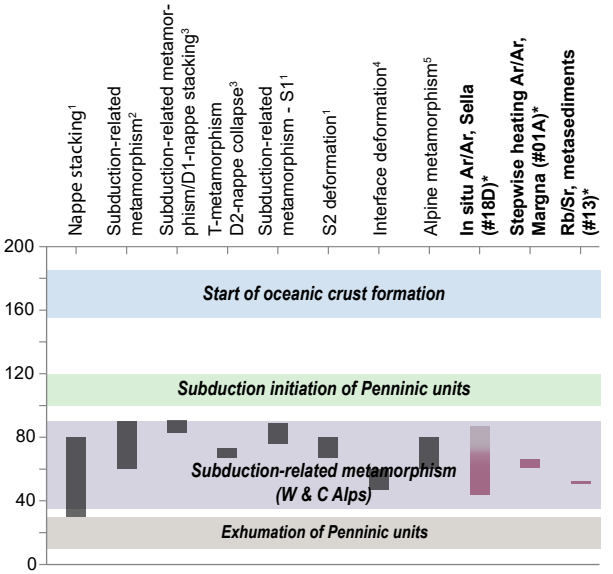

Figure 3. Published Alpine deformation age data for Val Malenco and Central Alps. Footnotes: (1) Handy et al. (1996); (2) Handy and Oberhänsli (2004); (3) Villa et al. (2000); (4) Bachmann et al. (2009b); (5) Frey et al. (1974); (*) this study.

ANALYTICAL METHODS

Electron Probe Microanalyses

Electron probe microanalyses (EPMA) were performed with a JEOL-JXA 8230 probe at GFZ Potsdam, under common analytical conditions (15 kV, 20 nA, wavelength-dispersive spectroscopy mode), using a 10-µm-diameter beam. The following standards were used for calibration: orthoclase (Al, Si, K), fluorite (F), rutile (Ti), Cr_2O_3 (Cr), wollastonite (Ca), tugtupite (Cl), albite (Na), MgO (Mg), Fe_2O_3 (Fe), rhodonite (Mn). Samples of micaschists and (ortho- and para-) gneisses were analyzed from both the Margna and Sella units. The analyses focused on phengite and to a lesser extent on amphibole composition of eight samples. The Si content per formula unit (pfu) of phengites (Ph) and the related content of the celadonite (Cel) end-member, $K(Mg,Fe^{2+})AlSi_4O_{10}(OH)_2$, are used here as an indicator of relative pressure changes (Massonne and Schreyer, 1987). In other words, high-silica regions of phengite correlate with lower aluminum contents and can be an indicator of relatively higher pressure conditions. Mineral abbreviations are used as suggested by Whitney and Evans (2010).

Thermodynamic Modeling

In order to estimate the P-T conditions under which micaschists and mica-rich gneisses from Magna shear zone (MSZ) and Intra-Sella shear zone (ISSZ) deformed, we calculated pseudosections, following a free-energy minimization approach using the software PerpleX (Connolly, 2005, version 6.7.7). The bulk rock composition in oxide weight percent was obtained by averaging for each sample conventional major elements X-ray fluorescence analyses on rock powders (made at the GFZ Potsdam) together with scanning electron microscope (SEM) surface estimates on thin sections (using an EVO MA-10 Zeiss microscope at the Institut de Physique du Globe de Paris [IPGP]). Synthetic bulk compositions used for the modeling as well as P-T pseudosection results are given in Supplemental Items S1 and S3–S5[1], respectively. The following solid solution models have been used for the modeling: phengite, garnet, amphibole (Holland et al., 1998), feldspar (Fuhrman and Lindsley, 1988), and chlorite (Holland et al., 1998). MnO has been considered only for samples #01B and #23B. Ferric iron has been neglected as suggested by the low-Fe content of clinozoisite crystals in the main Alpine foliation. Water is considered as pure H_2O and in excess in the system based on microstructural observations (presence of veins and pressure solution fringes).

Best-fit P-T regions for each pseudosection have been estimated considering: (1) the field where we had the best agreement between observed and modeled paragenesis; (2) the microstructural mechanical behavior of quartz and albite, which has been used as an approximate geothermometer; and (3) the phengite silica content isopleths.

Rb/Sr Geochronology

Ages of metamorphism and ductile deformation are herein investigated by Rb/Sr multi-mineral isochron dating for four mica-rich mylonites and one impure meta-carbonate. In this study, white mica is the high Rb/Sr phase, largely determining

SUPPLEMENTAL ITEM S1. XRF BULK ROCK CHEMICAL ANALYSES

Sample	SiO2 (%)	TiO2 (%)	Al2O3 (%)	Fe2O3 (%)	MnO (%)	MgO (%)	CaO (%)	Na2O (%)	K2O (%)	P2O5 (%)	LOI Tiegel (%)	Sum (%)
#01A	68.5	0.450	15.7	3.00	0.031	1.00	0.71	4.35	3.91	0.221	1.84	99.70
#01B	80.5	0.364	7.9	3.35	0.038	1.36	1.04	0.16	2.14	0.215	2.62	99.61
#23B	59.1	0.794	18.2	8.19	0.108	3.16	0.65	2.52	3.67	0.152	2.68	99.28

	Ba (ppm)	Cr (ppm)	Ga (ppm)	Nb (ppm)	Ni (ppm)	Rb (ppm)	Sr (ppm)	V (ppm)	Y (ppm)	Zn (ppm)	Zr (ppm)
#01A	922	23	19	14	<10	123	94	37	42	27	202
#01B	385	458	12	<10	19	85	165	609	54	51	88
#23B	2697	98	22	13	32	121	72	124	33	123	138

SUPPLEMENTAL ITEM S2. ANALYTICAL DATA OF Rb/Sr GEOCHRONOLOGY

Sample no. / Analysis no.	Material	Rb (ppm)	Sr (ppm)	$^{87}Rb/^{86}Sr$	$^{87}Sr/^{86}Sr$	$^{87}Sr/^{86}Sr$ $2\sigma_m$ (%)
#01A (disequilibria; maximum age* = 44.0 ± 0.74 Ma)						
PS2840	wm 125-90 µm	209	61.5	9.86	0.725047	0.0018
PS2838	apatite	5.88	2410	0.00706	0.718988	0.0011
PS2839	feldspar	9.33	82.5	0.328	0.718093	0.0025
PS2840	wm 125-90 µm	209	61.5	9.86	0.725047	0.0018
PS2841	wm 355-250 µm	307	26.7	33.3	0.748662	0.0016
PS2842	wm 500-355 µm	306	30.9	28.8	0.744595	0.0022
#01F (disequilibria; maximum age* = 54.3 ± 1.1 Ma)						
PS2825	feldspar	2.9	65.1	0.129	0.713050	0.0027
PS2826	wm 355-250 µm	347	218	4.60	0.716726	0.0018
PS2827	wm 500-355 µm	350	213	4.75	0.716893	0.0020
PS2828	wm 125-90 µm	296	175	4.90	0.716674	0.0022
PS2829	wm 250-125 µm	331	203	4.73	0.716662	0.0014
PS2830	apatite	0.48	1652	0.00085	0.712138	0.0013
PS2831	titanite	1.43	66.7	0.062	0.710473	0.0010
#02 (disequilibria; maximum age* = 78.9 ± 1.8 Ma)						
PS2832	feldspar	13.6	30.6	1.29	0.730217	0.0014
PS2833	wm 125-90 µm	299	158	5.49	0.734855	0.0018
PS2834	wm 500-355 µm	355	166	6.20	0.736391	0.0012
PS2835	apatite	1.89	1479	0.0037	0.728496	0.0023
PS2836	wm 355-250 µm	364	170	6.22	0.736267	0.0012
PS2837	wm 250-125 µm	360	172	6.06	0.735831	0.0016
#23B (disequilibria; 184 ± 71 Ma)						
PS2819	wm 500-355 µm	359	69.9	14.9	0.766369	0.0018

* max. age refers to the maximum age for the end of deformation.

[1]Supplemental Items. Item S1: X-ray fluorescence bulk-rock chemical analyses. Item S2: Analytical data of Rb/Sr geochronology. Item S3: Pressure-temperature pseudosection in the NCKFMASH system (plus Qz and water) for sample #01A, showing the phase relationships and the best-fit area (red polygon). Item S4: Pressure-temperature pseudosection in the Mn-NCKFMASH system (plus Qz and water) for sample #01B, showing the phase relationships and the best-fit area (red polygon). Item S5: Pressure-temperature pseudosection in the NCKFMASH system (plus Qz and water) for sample #23B, showing the phase relationships and the best-fit area (red polygon). Please visit https://doi.org/10.1130/GES02149.S1 or access the full-text article on www.gsapubs.org to view the Supplemental Items.

the calculated age values. The Rb/Sr system of white mica is thermally stable at temperatures up to >600 °C (Glodny et al., 2008a) but may be fully reset by dynamic recrystallization even at lower temperature, down to 350 °C. Moreover, complete synkinematic recrystallization is often accompanied by inter-mineral isotopic re-equilibration (Inger and Cliff, 1994; Freeman et al., 1997; Villa, 1998; Müller et al., 1999, 2000; Cliff and Meffan-Main, 2003; Glodny et al., 2008b). Therefore, Rb/Sr isotopic data from penetratively deformed rocks can be used to date the waning stages of mylonitic deformation, given that deformation occurred below the temperature range for diffusional resetting and that no later substantial reheating or fluid-rock interaction occurred.

For Rb/Sr geochronology, mineral separates from three basement rock samples from the Margna nappe, one basement rock sample from the Sella nappe, and one from the meta-sediments covering the aforementioned pre-Alpine basement rocks have been prepared (see Table 1), with different mica grain-size fractions to identify possible presence of mixed mica populations (i.e., presence of unequilibrated, detrital, pre- or early deformational white mica relics; Müller et al., 1999). Isotopic data were generated at GFZ Potsdam using a Thermo Scientific TRITON thermal-ionization mass spectrometer. Sample processing, mineral separation, and data acquisition were performed following the procedures reported in Glodny et al. (2008a). Uncertainties of Rb/Sr isotope and age data are quoted at the 2σ level throughout this work. The software Isoplot/Ex 3.71 (Ludwig, 2009) and the revised Rb decay constant of $1.3972*10^{-11}$ yr^{-1} (Villa et al., 2015) were used to calculate regression lines. The full Rb/Sr data set is presented in Supplemental Item S2 (footnote 1).

$^{40}Ar/^{39}Ar$ Dating

$^{40}Ar/^{39}Ar$ dating was performed at the $^{40}Ar/^{39}Ar$ geochronology laboratory of Potsdam University. Bulk mineral separates $^{40}Ar/^{39}Ar$ dating and in situ $^{40}Ar/^{39}Ar$ UV laser ablation dating were performed on one mica-rich mylonitic sample from the Margna nappe and one foliated cataclastic micaschist sample from the Sella nappe, respectively. For the first technique, $^{40}Ar/^{39}Ar$ dating of bulk mineral separates by CO_2 laser stepwise heating, one hand specimen of micaschist was crushed and sieved. White mica fractions were obtained (handpicked fractions of 355–250 µm and mechanically prepared fractions of 500–355 and 355–250 µm; see also Wiederkehr et al., 2009 for fraction preparation) with a total of ~10 mg of white mica. Scanning electron microscope investigations were performed for this sample, in order to make sure that no chemical zoning characterized white micas and hence the ages would reflect more likely deformation-induced recrystallization. For in situ $^{40}Ar/^{39}Ar$ dating by UV laser ablation, a rock thick section (of ~1 mm thickness and 5 mm diameter) was prepared and double polished. Before the laser experiment, the thick section was studied using the SEM in order to have an accurate reference frame during the $^{40}Ar/^{39}Ar$ experiment and a general control over mica zoning patterns.

The $^{40}Ar/^{39}Ar$ analytical system at the University of Potsdam has been described in detail in recent studies (Wiederkehr et al., 2009; Wilke et al., 2010; Halama et al., 2014). The Ar isotopic analytical system consists of (1) a New Wave Gantry Dual Wave laser ablation system with a 50 W continuous CO_2

TABLE 1. OVERVIEW OF SAMPLES AND LOCATIONS

Sample	Location	Latitude (°N)	Longitude (°E)	Rock	Minerals
Margna					
#01A	Rifugio Carate Brianza	46°19′57.26″	09°54′14.05″	Gneiss	Qz-Ab-Wm-Ttn-Ap-Aln-Px-Zrn
#01B	Same as above	Same as above	Same as above	Micaschist	Qz-Wm-Chl-Grt-Bt-Hbl-Ap-Mag-Aln-Ep
#01F	Same as above	Same as above	Same as above	Micaschist	Qz-Wm-Fsp-Chl-Ep
#02	Forca di Fellaria	46°19′44.97″	09°55′10.42″	Micaschist	Qz-Fsp-Wm-Chl
Sella					
#11B	Alpe Gembre	46°19′42.50″	09°57′54.50″	Gneiss	Qz-Fsp-Wm-Chl
#18D	Rifugio Marinelli	46°20′49.30″	09°54′11.70″	Micaschist	Qz-Wm-Chl-Ttn-Rt-Ilm
#23B	Same as above	Same as above	Same as above	Micaschist	Qz-Ab-Wm-Chl-Zrn-Ttn-Aln-Rt
#8.1	Rifugio Bignami	46°20′27.97″	09°56′41.39″	Gneiss	Qz-Pl-Wm-Chl-Ap-Ep-Zrn
#8.2.1	Same as above	Same as above	Same as above	Gneiss	Qz-Pl-Wm-Rt
#8.2.2	Same as above	Same as above	Same as above		Qz-Fsp-Wm-Chl-Amp(Act-Hbl)-Hem-Ttn-Ep-Bt
#8.3.2	Same as above	Same as above	Same as above	Gneiss	Qz-Pl-Ep-Ttn
Metasediments					
#13	Rifugio Bignami	46°19′28.30″	09°58′08.40″	Marbles	Cal-Qz-Wm

laser (wavelength of 10.6 mm) for heating bulk samples and also Nd-YAG UV laser (frequency-quadrupled wavelength of 266 nm) for laser ablation of the thick section samples for extracting sample gases; (2) an ultra-high vacuum purification line equipped with two SAES getters and a cold trap used at –90 °C; and (3) a high-sensitivity Micromass 5400 noble gas mass spectrometer equipped with an electron multiplier. The analysis with Micromass 5400 has been done with MassSpec software manufactured by Dr. Alan Deino in the Berkeley Geochronology Center, California, USA.

Neutron activation of both samples was performed at the CLICIT Facility of the Oregon State University TRIGA Reactor, in Corvallis, Oregon, USA. All of the unknown samples were wrapped in commercial Al foil and were then contained in a 99.999% pure Al sample container (22.7 mm in diameter and 102.5 mm in height), together with the neutron flux monitoring mineral, Fish Canyon Tuff sanidine, prepared by the Geological Survey of Japan (Uto et al., 1997; Ishizuka, 1998; 27.5 Ma) and crystals of K_2SO_4 and CaF_2 for correction of interference by Ar isotopes produced from K and Ca other than those produced by $^{39}K(n,p)^{39}Ar$ reaction. The container had been irradiated for 4 h with the fast neutron flux of 2.5×10^{13} n/cm^2/s. After storage of the samples for several weeks at the reactor, they were finally brought back to Potsdam and then were analyzed for Ar isotopes. A K-Ar age standard biotite, HD-B1 biotite (Schwarz and Trieloff, 2007; 24.18 ± 0.09 Ma), which was also included in the same Al sample container as a routine procedure for every irradiation, was analyzed, and the accuracy of the system was confirmed.

RESULTS

Field Observations

The studied area comprises a series of several hectometer- to kilometer-thick continental slivers (pre-Alpine orthogneisses and micaschists) separated by greenschist-facies ductile shear zones. Some of these slices locally exhibit well-preserved magmatic fabrics, in particular in the Sella nappe. Anastomosing deformation networks are visible in the cliffs as well as in the landscape: they form 5–10-m-thick shear zones generally subparallel to the main Alpine shear zones. One of the major shear zones of the studied sequence lies within the lowermost 200 m at the base of the Margna nappe at the contact with the Malenco unit. Sheared metagranitic rocks exhibit a main foliation affected by a crenulation cleavage (Fig. 4A). Clasts of silica-rich domains (probably former pegmatitic veins in the orthogneiss) are observed wrapped by the main proto-mylonitic foliation (Fig. 4B). Semi-brittle deformation networks, marked in the field by broken feldspar clasts in a weakly oriented matrix are either found along the main thrust contacts or distributed within Margna and Sella slices (Fig. 4C). Along both the basal Margna shear zone (MSZ) and the Intra-Sella shear zone (ISSZ), foliated cataclasites (Fig. 4D) comprising submillimeter- to millimeter-sized clasts are exposed. Several generations of foliated cataclasites are recognized, striking parallel to the main N-plunging foliation or slightly oblique to it. They form centimeter- to decimeter-sized networks interleaved with domains where semi-brittle and ductile deformation prevails. Centimeter-thick quartz veins are locally observed within the regions more affected by Alpine deformation. Quartz veins are either found as en echelon vein sets cutting at high angle the main foliation (Fig. 4E) or as boudinaged lenses wrapped by the alpine foliation (Fig. 4F). A very strong flattening recorded in rock microfabrics contributed to the formation of numerous pressure-solution fringes visible from hand specimen to millimeter scale in both orthogneisses and Sella nappe micaschists (Fig. 4G).

Kinematic indicators, obscured by the strong flattening, indicate mixed top-N and top-SE tectonic transport directions. Previous studies in the broader Penninic/Austroalpine boundary report top-W kinematics during Cretaceous and a later shift to mainly top-N (e.g., Ratschbacher, 1986; Ring et al., 1988, 1989; Liniger and Nievergelt, 1990). However, it is possible that, locally, the old top-W structures are overprinted by the second phase; such is the case in Middle Austroalpine units of the Eastern Alps where transport directions are mainly top-N, although locally E-W stretching directions are observed (Ratschbacher, 1986). We recognized such top-W kinematic indicators in the Maloja gneiss NW of our study area, in Maloja pass, but not in the Val Malenco.

The top of the basal Margna shear zone is lined by an extremely sheared, nearly continuous ribbon lens of impure marbles forming mylonites and brecciated dolomitic limestones (Fig. 4H), while pseudotachylytes are commonly found in loose blocks falling from inaccessible cliffs that probably form the Sella and Bernina units (Fig. 4I).

Ductile deformation in the Malenco Massif led to pervasive mylonitic deformation of antigorite schists. The strong compositional and deformational gradient along the basal Margna shear zone between the crustal and mantle materials locally led to the formation of a metasomatized tectonic mixing zone comprising lenses of mafic tuffs, submetric to metric lenses of metasediments, as well as minor volumes of tremolite schists, and in parts deformed basement rocks exhibiting foliated cataclasites (named "breccias" in Picazo et al., 2019).

Petrographic Description

Continental Austroalpine rocks for petrographic and geochronological studies were carefully selected based on the greatest intensity of Alpine overprint. In less mylonitized facies, few remnants of the pre-Alpine assemblages, namely albite porphyroclasts (Fig. 5A), garnet cores (Fig. 5E), biotite flakes, hornblende cores, and (possibly alpine prograde) muscovite cores can be observed. Alpine deformation led to the formation of a fine-grained foliation underlined by oriented phengite planes (Fig. 5A), tremolite around hornblende, clinozoisite, and titanite neoblasts (Fig. 5F). Pressure-solution fringes line up the main foliation. In one foliated cataclasite sample, two crosscutting foliations were observed (Figs. 5B and 5G), possibly associated with two stages of deformation, i.e., one that formed the main foliation and one that formed coevally with the crenulation cleavage. In quartz-rich lithologies, a strong apparent crystal-preferred orientation (CPO) denotes the existence of dynamic

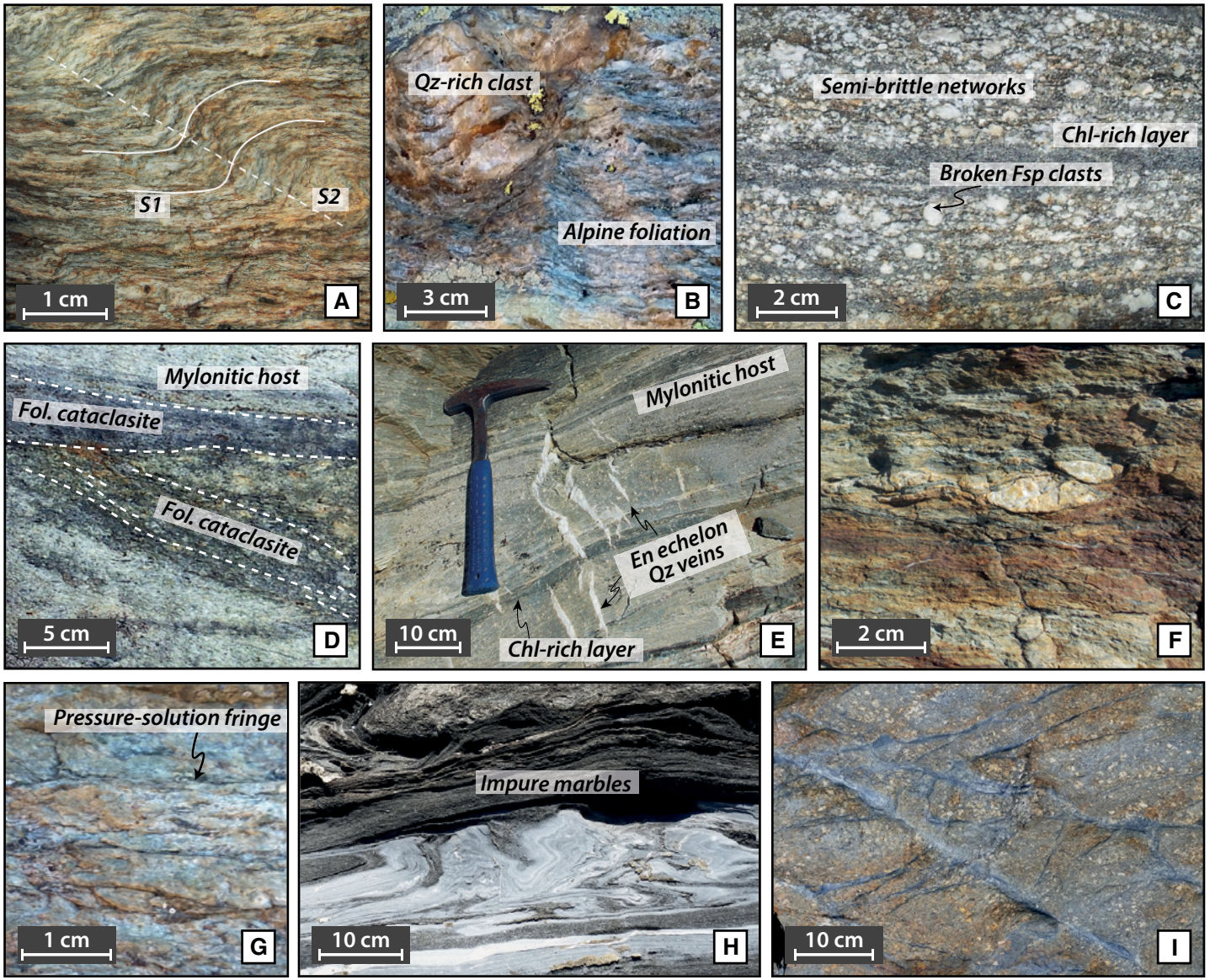

Figure 4. (A) Representative view of the Alpine imprint in Margna nappe gneisses showing a main foliation (S1) moderately imprinted by a crenulation plane (S2). (B) Field picture showing a silicic clast (former magmatic vein?) wrapped in the alpine foliation in the basal Margna shear zone. (C) Field picture showing a semi-brittle network comprising numerous finely crushed feldspar clasts moderately sheared along the main foliation (Sella nappe). (D) Picture showing two crosscutting generations of finely fractured orthogneisses (foliated cataclasites; Sella nappe). (E) Picture showing the mylonitic foliation from the Intra-Sella shear zone crosscut by en echelon quartz veins. (F) Picture showing centimeter-thick quartz vein as a boudinaged lens. (G) Close-up hand specimen picture showing the presence of darkish pressure solution planes, mostly parallel to the main thrust fault. (H) Layers of marbles and impure marbles showing tight folds (base of the Margna nappe). (I) Block deriving possibly from Sella or Bernina nappe, showing networks of pseudotachylytes (black veins) crosscutting a weakly deformed dioritic matrix.

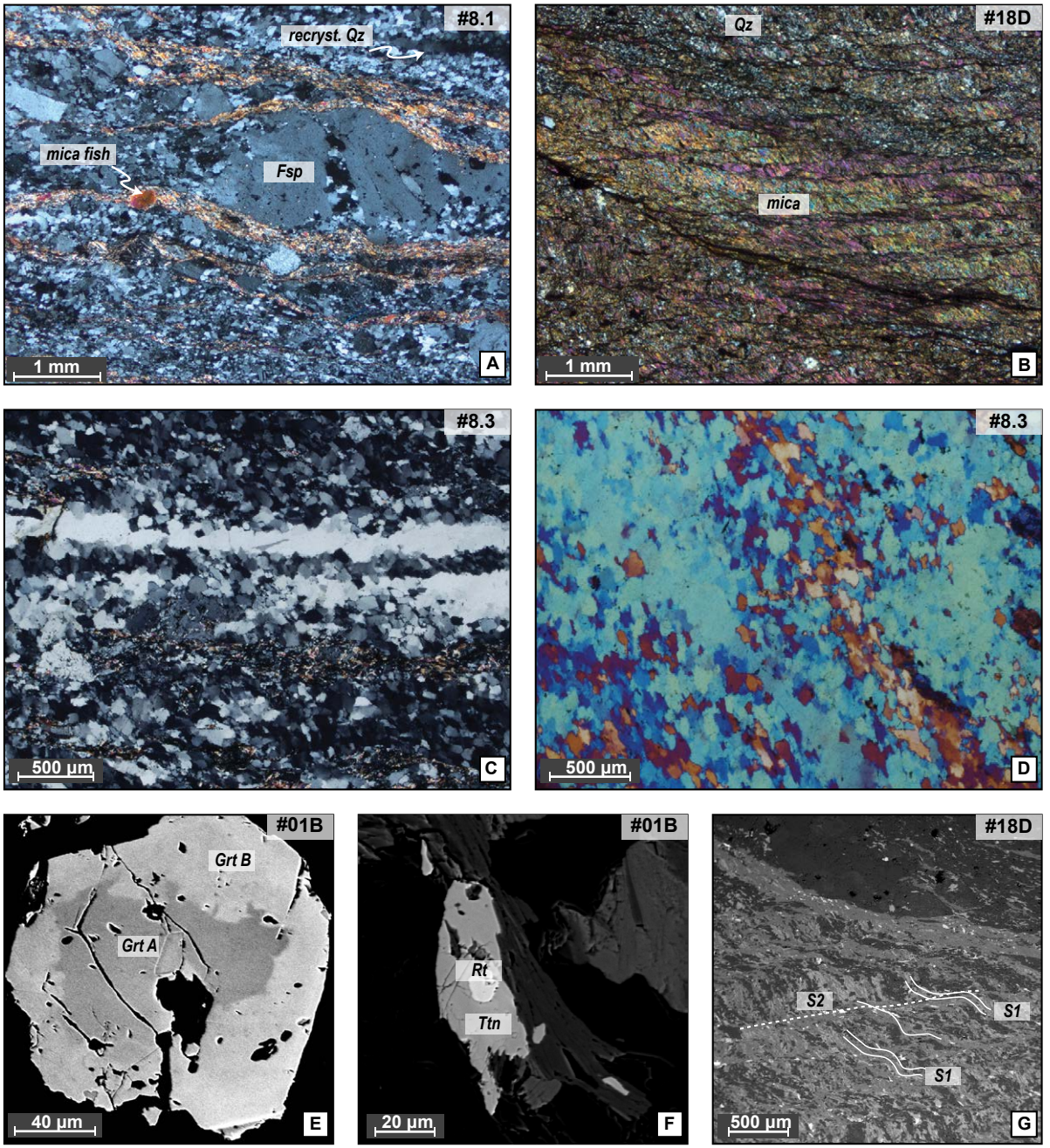

Figure 5. (A) Optical microscope view (with polarized light) of a Sella mylonite showing a feldspar boudin, wrapped by micas, which mark the foliation. The feldspar grain has been partly replaced by quartz. A big white mica grain, within the fine mica foliation shows partial recrystallization of white micas. Quartz is recrystallized in the whole thin section. (B) Optical microscope view (with polarized light) of a Sella micaschist. The fine-grained micas form two foliations, S1 and S2 (see also picture G in the same figure). (C) Recrystallized quartz from a Sella mylonite, exhibiting recrystallization ribbons (with polarized light). (D) Crystal-preferred orientation (CPO) in recrystallized quartz from Sella mylonite (polarized light + gypsum plate). (E) Backscatter electron image of a garnet, with two distinct compositions; Margna mylonite. (F) Backscatter electron image showing titanite rimming around rutile in Sella micaschist. (G) Backscatter electron image of a Sella micaschist, showing the two different foliations, S1 and S2.

recrystallization during shearing (Figs. 5C and 5D). On the contrary, albite does not show clear evidence of intracrystalline deformation.

In samples identified as foliated cataclasites, all the mineral phases including albite and quartz exhibit microfracturing and alignment of crystal clasts along discrete shear planes. The semi-brittle networks differ from foliated cataclasites by the presence of coeval crystal-plastic deformation along shear planes (mostly underlined by phyllosilicates) and micro-cracking of stronger albite grains. Phengite planes are commonly closely associated with chlorite (Figs. 6A and 6B). Relicts of pre-Alpine origin exhibit micro-fracturing and resorption textures (Fig. 6D). In some mylonitic samples, quartz exhibits marked grain size reduction.

Samples from both MSZ and ISSZ reveal the presence of Al-rich/Si-poor white mica cores (Si ~3.2 pfu; Fig. 6A), surrounded by Al-poor/Si-rich phengitic mantles (Si between 3.3 and 3.4 pfu; Fig. 6C; Table 2). Phengite outer rims thus do not exhibit systematically lower Si contents as may be the case when phengite recrystallizes at lower pressure conditions during exhumation. The average Si content of the basal Margna shear zone is ~3.22 pfu, and the maximum Si content is 3.32 pfu, both slightly lower than those of Guntli and Liniger (1989). The respective values for the Intra-Sella shear zone are ~3.31 pfu (average) and 3.46 pfu (maximum). Depending on the intensity of the Alpine overprint, the proportion of fully recrystallized phengite crystals ranges from 20 vol% (e.g., #01B; Fig. 6A) to nearly 90 vol% in #18D (Fig. 6B). Only one sample (#01B) exhibits thin Fe-rich garnet rims around a partly corroded, darker garnet core (Figs. 5E and 6D). The core of this garnet has a significantly higher XMg (Mg/(Fe + Mg)) content than its rims (Fig. 6E). A summary of our petrographic observations is presented in Figure 6F and Table 1; representative mineral analyses are shown in Table 2.

Thermodynamic Modeling Results

Best-fit region between observed parageneses and the modeled system is obtained at 0.9–1.0 GPa and 350–375 °C for sample #23B, while slightly lower pressures and higher temperatures correspond to sample #01A (0.65–0.9 GPa and 350–400 °C). The corresponding mineral assemblages predicted by the model are the following: Ab-Ph-Qz-Chl-Ep-Ttn-Pg and Ab-Ph-Qz-Chl-Ep-Ttn-Amp, for sample #23B and #01A, respectively. Even lower pressure and higher temperature conditions were obtained for #01B (0.6–0.9 GPa, ~450 °C; Fig. 7), corresponding to a paragenesis composed of Qz-Fs-Ph-Chl-Amp-Grt-Ep-Ttn. Detailed pseudosection plots are provided in Supplemental Items S3–S5 (footnote 1). Modeled mineral modes are in agreement with observed modes in the samples. Note that the pressure estimates derived from the pseudosection modeling strongly depend on the position of the phengite silica isopleths, which represent the most reliable barometer for such an assemblage.

Geochronological Results

Rb/Sr Dating

Determination of deformation ages from Margna and Sella basement rocks proved problematic because of Sr-isotope disequilibria in the mica populations. Smaller grains appear to be systematically younger than bigger grains (Figs. 8B and 8C). This pattern is a characteristic signature of incomplete recrystallization. Correspondingly, all basement rock samples show disequilibria among the low–Rb/Sr phases (apatite, feldspar, and titanite). The issue of isotopic heterogeneity due to inheritance has been extensively addressed in Glodny et al. (2005) and highlighted in Bachmann et al. (2009b) and Angiboust et al. (2014). Full recrystallization of white mica during deformation together with Sr-bearing phases (such as apatite or albite) yields Sr isotopic re-equilibration, and ages calculated from equilibrated (sub)assemblages generally reflect the waning stages of deformation (e.g., Freeman et al., 1998; Inger and Cliff, 1994). In our samples, full recrystallization of pre-Alpine basement rocks was obviously not achieved, and Alpine, exhumation-related temperatures in our samples were too low for diffusional resetting. The only geologically meaningful ages that could be calculated are ages of ca. 44 and 54 Ma, interpreted as maximum ages for the end of deformation for samples #01A and #01F, respectively (see also Discussion and Interpretation of Age Data sections for explanation of our observed data ranges).

Since dating of the pre-Alpine basement rocks did not produce conclusive results, we analyzed and dated a sample from the meta-sedimentary rocks found between the Margna and the Sella nappes. Despite small disequilibria between different calcite-dominated rock fragments, robust age information of 48.9 ± 0.9 Ma was acquired. Notably, for this sample, no correlation between mica grain size and apparent age is observed (Fig. 8A). Therefore, although the Alpine overprint in the study area cannot be precisely dated with Rb/Sr in white micas of pre-Alpine rocks, dating white micas from meta-sediments devoid of pre-Alpine history facilitates dating of the waning stages of ductile deformation. Analytical data on Rb/Sr geochronology are given in Supplemental Item 2 (footnote 1).

$^{40}Ar/^{39}Ar$ Dating

Here we present the results acquired during stepwise heating as well as in situ $^{40}Ar/^{39}Ar$ dating on one mylonitic orthogneiss from Margna and one foliated cataclasite from Sella. The complete set of isotopic data is presented in Tables 3 and 4 for stepwise heating and in situ $^{40}Ar/^{39}Ar$ dating, respectively.

Stepwise heating. Stepwise-heating $^{40}Ar/^{39}Ar$ analysis was performed for mica fractions of mylonitic sample #01A (right column of Fig. 8B). Microscopically, the sample exhibits flattened quartz and mica flakes, the latter co-defining the foliation. There are no apparent core-rim structures in the dated micas; therefore, deformation is thought to have affected them homogeneously. Dating of this sample yielded fairly homogeneous apparent ages for all grain sizes, namely a range of apparent deformation ages between 61.1 and 66.2 (±0.3) Ma (Figs. 9A–9C). In particular, although an apparent plateau age for the handpicked small fractions (#01A–H, 355–250 µm) was not detected, most steps point to a meaningful age of ca. 66–64

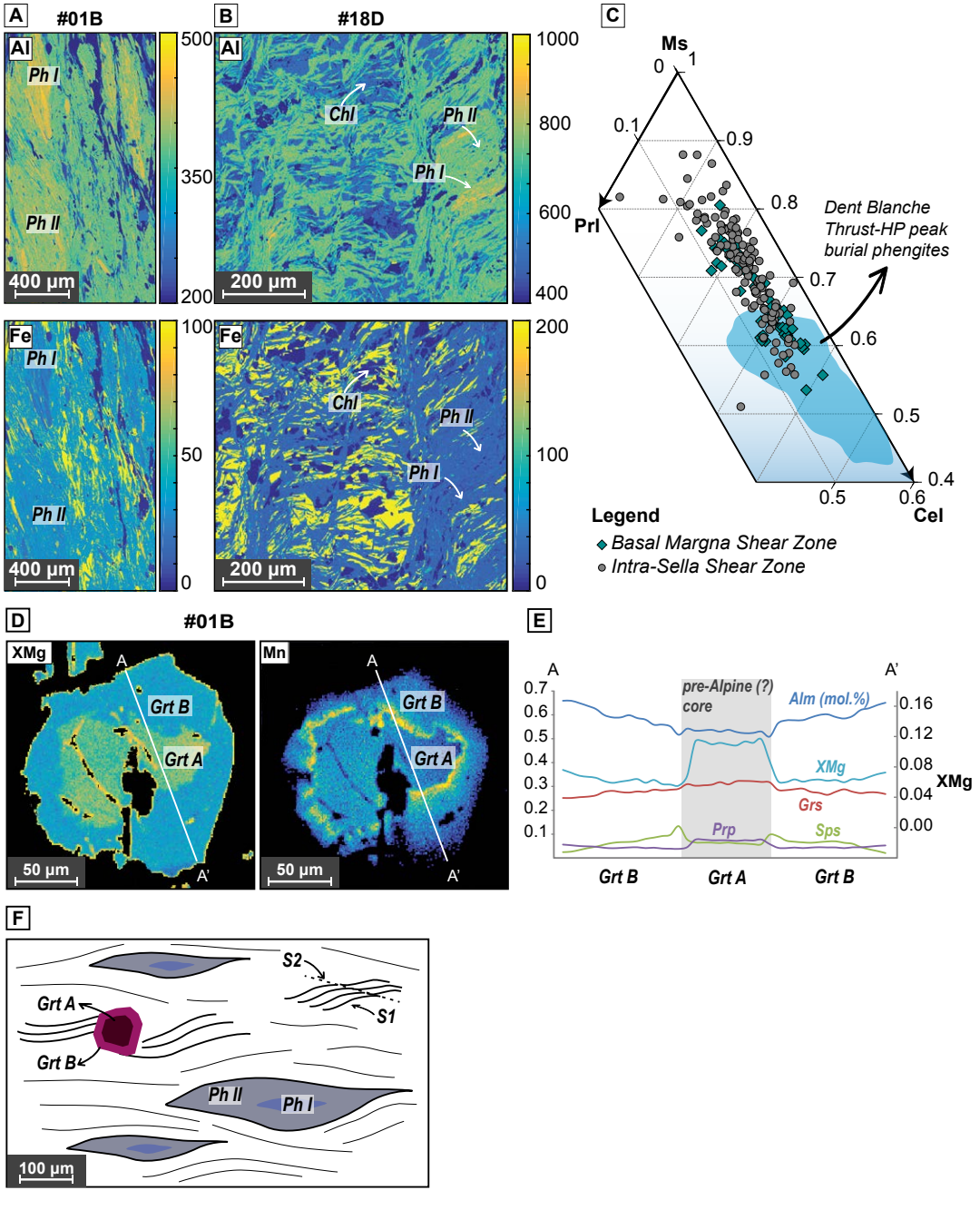

Figure 6. (A) X-ray map of a mica-rich shear band from sample #01B showing that the matrix mainly composed of a high-pressure phengitic mica foliation (Ph II), locally contains 200–300 mm large remnants of higher aluminum clasts (Ph I). Chlorite flakes intergrown with phengite are best visible on the Fe map. (B) X-ray map of a mica-rich shear band from sample #18D showing chlorite-phengite domain. (C) Triangular plot of phengite composition in the celadonite-pyrophyllite-muscovite system for samples from the two shear zones studied here. The blue shaded domain shows, for comparison, the composition of peak burial phengite analyses from the Dent Blanche Massif (data from Angiboust et al., 2014, 2015). (D) X-ray map of a garnet crystal from sample #01B showing two distinct compositions: the core (Grt A) clearly evidences resorption and overgrowth by a newly formed generation (Grt B). The end-member compositions corresponding to the transect A–A' are shown in Figure 6E. (E) Composition profile across the garnet crystal shown in Figure 6D. Note the presence of a high Mn content at the contact between the (possibly) pre-Alpine and the alpine generation. (F) Schematic representation of the microstructures observed in sample #01B, showing the foliation, the two phengite generations, the core-rim structure of the garnet shown in Figure 6D and S1-S2 structures. Alm—almandine; Grs—grossular; Prp—pyrope; Sps—spessartine.

TABLE 2. MINERAL CHEMICAL ANALYSES FOR GARNET, AMPHIBOLE, AND PHENGITES FROM MARGNA AND SELLA NAPPES

	Garnet	Garnet	Amphibole	Phengite	(nOx = 11)								
Sample:	#01B	#01B	#8.2.2	#01B	#01B	#02	#02	#11B	#11B	#18D	#18D	#23B	#23B
Reference:	Z1-1-L18	Z1-1-L34	Z1-19	All (23)	Z2-8	All (16)	Z3-1	All (38)	Z1-5	All (51)	Z1-2	All (34)	Z2-7
Structure:	Core	Rim	Core	Avg.	Max.*	Avg.	Max.*	Avg.	Max.*	Avg.	Max.*	Avg.	Max.*
SiO_2	37.38	37.28	45.01	48.00	49.74	47.79	48.13	48.70	46.70	48.73	49.63	49.94	52.61
TiO_2	0.09	0.19	1.20	0.44	0.36	0.29	0.33	0.27	0.25	0.19	0.12	0.31	0.38
Al_2O_3	20.79	20.70	9.63	29.69	29.10	32.28	31.49	29.76	29.85	30.29	29.29	27.38	26.49
FeO	24.88	26.97	18.62	3.18	2.74	2.29	2.42	2.49	2.69	2.82	2.64	3.68	1.99
MnO	2.97	3.15	0.66	0.01	0.02	0.00	0.01	0.01	0.01	0.02	0.01	0.03	0.01
MgO	2.01	1.13	9.13	2.41	2.58	1.58	1.81	2.59	2.45	2.31	2.72	3.23	3.77
CaO	11.06	9.90	11.62	0.02	0.03	0.01	0.00	0.01	0.01	0.03	0.03	0.03	0.01
Na_2O	0.00	0.00	1.43	0.65	0.50	0.72	0.82	0.53	0.47	0.27	0.19	0.14	0.19
K_2O	0.00	0.00	0.72	9.91	10.26	9.74	9.70	10.22	10.30	10.41	10.79	10.78	10.78
Sum	99.18	99.33	98.03	94.32	95.33	94.70	94.70	94.58	94.73	95.07	95.43	95.52	96.26
Si	2.99	3.00	6.74	3.25	3.32	3.20	3.23	3.30	3.39	3.27	3.32	3.35	3.46
Ti	0.01	0.01	0.14	0.02	0.02	0.01	0.02	0.01	0.02	0.01	0.01	0.02	0.02
Al	1.96	1.97	1.70 (tot)	2.37	2.29	2.55	2.49	2.32	2.17	2.39	2.31	2.17	2.06
Fe_{tot}	1.67	1.82	2.30	0.18	0.15	0.13	0.14	0.16	0.16	0.16	0.15	0.20	0.11
Mn	0.20	0.21	0.08	0.00	0.00	0.00	0.00	0.00	0.00	0.00	0.00	0.00	0.00
Mg	0.24	0.14	2.04	0.24	0.26	0.16	0.18	0.27	0.30	0.23	0.27	0.32	0.37
Ca	0.95	0.85	1.86	0.00	0.00	0.00	0.00	0.00	0.00	0.00	0.00	0.00	0.00
Na	0.00	0.00	0.42	0.08	0.06	0.09	0.11	0.06	0.02	0.03	0.03	0.02	0.02
K	0.00	0.00	0.14	0.86	0.87	0.83	0.83	0.89	0.92	0.89	0.92	0.92	0.91
XPrp	8.00	4.00	XMg	0.60	0.62	0.55	0.57	0.64	0.65	0.59	0.65	0.62	0.77
XAlm	54.00	59.00	Ms	0.72	0.65	0.78	0.75	0.69	0.61	0.72	0.67	0.64	0.52
XSps	7.00	7.00	Cel	0.22	0.28	0.14	0.18	0.25	0.34	0.20	0.27	0.31	0.41
XGrs	31.00	28.00	Prl	0.06	0.07	0.08	0.07	0.06	0.06	0.08	0.06	0.05	0.07

*Chemical analysis with the maximum Si content (pfu) in the analyzed sample.

Ma (Fig. 9A). A plateau age of 64.6 (±0.3) Ma was obtained for small fractions (#01A–L, 355–250 µm), collected by mechanical means (Fig. 9B). Finally, stepwise-heating dating of large mica fractions collected by the same method (#01A-P, 500–355 µm) varies from ca. 55 Ma to ca. 61 Ma, therefore exhibiting an irregular pattern (Fig. 9C).

In situ dating. Macroscopically, sample #18D appears to be a foliated cataclasite, while its microstructure is characterized by the presence of S-C fabric in micas and large boudins of quartz. Foliation in the sample is marked by interconnected and synkinematic white micas and chlorite, coinciding with the S-fabric. Based on the microstructural observations, two different structures of white mica were systematically dated: along the S-plane (blue color in Figs. 10A–10E) and along the C-plane (green color in Figs. 10A, 10B, 10E, and 10F). For the interpretation of the data, measurements with high Ca/K ratio were omitted, because Ca-derived ^{37}Ar was not produced in white micas but was derived from other Ca-rich minerals such as epidote and/or titanite, thus contamination of Ar from those Ca-rich minerals could be considered. Finally, we included only measurements that produced a total Ar of more than 40% of in situ radiogenic Ar and yielded an analytical uncertainty <5 Ma.

Ages span a wide range for white micas along S-planes, including micas wrapping around quartz. However, measurements with the lowest uncertainties were obtained for ages between 44.0 ± 2.3 and 70.7 ± 2.7 Ma (Fig. 10G; Table 4). Due to their smaller extended length in the sample, fewer points were measured for micas forming the C-structures, which yielded intermediate ages from 56.0 ± 1.2–70.1 ± 3.0 Ma (Fig. 10G; Table 4). Since there is an overlap of ages for both structures, we cannot attribute them to separate kinematic or deformational events. It is interesting, however, to notice that the maximum ages obtained from Rb/Sr for the end of Alpine deformation (44.0 ± 0.7 and 54.3 ± 1.1 Ma) coincide with the youngest ages obtained by in situ $^{40}Ar/^{39}Ar$ dating.

DISCUSSION

Interpretation of P-T Data

We herein provide a first attempt to quantify the pressure-temperature history for the Alpine overprint event in Austroalpine rocks from the

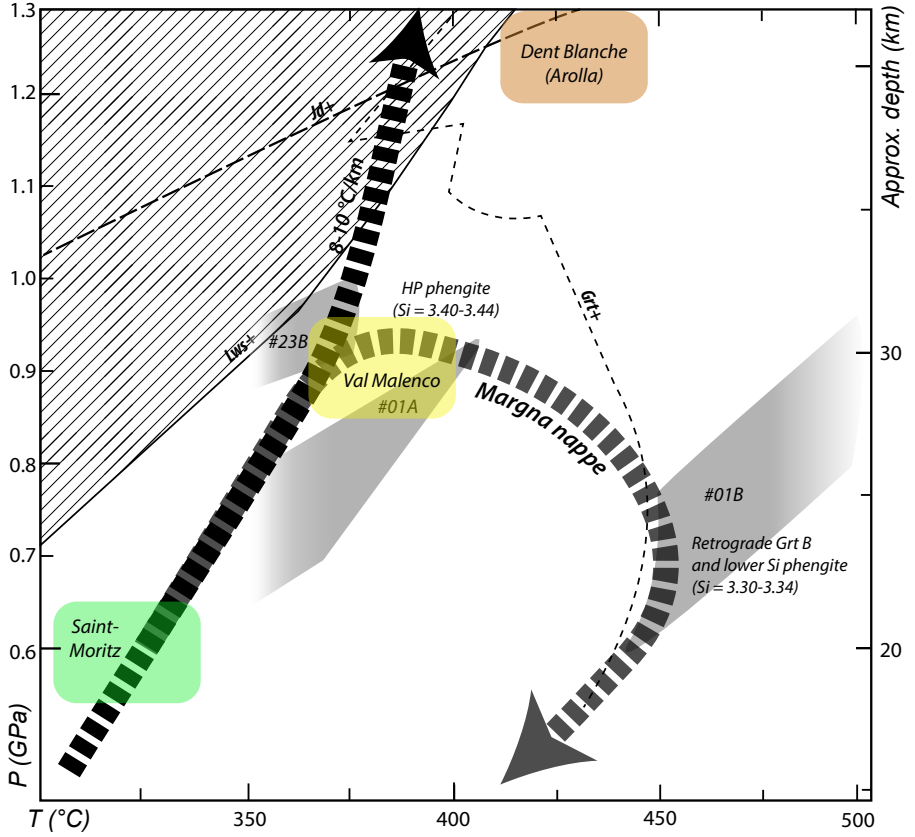

Figure 7. Summary of pseudosection modeling results comparing obtained results (gray shaded polygons) with peak burial estimates for the Arolla gneiss in Western Alps (brown rectangle; Angiboust et al., 2014) and the Austroalpine orthogneiss in St. Moritz (green rectangle; Bachmann et al., 2009b), both accreted along the same alpine paleo-interface (detailed pressure-temperature [P-T] pseudosections calculated for this work are provided in Supplemental Items S3, S4 and S5 [text footnote 1]). Gray-shaded polygons correspond to the best-fit areas identified for each individual sample peak burial conditions. The shape of the retrograde path is controlled by the retrogressed sample #01B and by the presence of garnet (Grt) in this sample. Jd—jadeite; Lws—lawsonite.

Malenco region. Synkinematic growth of chlorite and white mica and the recrystallization of quartz place a lower limit on temperatures at ~250 °C. Brittle deformation of albite as well as absence of blue amphibole and jadeite set an upper limit for peak T (<500 °C) and peak P conditions (<1.2 GPa). Moreover, our pseudosection results along with micro-fabrics analysis suggest that deformation during Alpine convergence took place at T > 350 °C and pressures ~0.9 GPa. This estimate plots along the burial gradient of 8°-10°/km commonly accepted for late Cretaceous Alpine metamorphism (e.g., Agard et al., 2001). These pressure-temperature estimates are in agreement with previous attempts to quantify the alpine metamorphism in the base of the Austroalpine stack farther to the NW in the Bivio region (Handy et al., 1996) and in the Piz de la Margna region (main Alpine foliation; Guntli and Liniger, 1989) where 0.6–0.9 GPa and 300–450 °C were obtained. A later stage of lower-pressure conditions is also mentioned for deformation postkinematic to the main Alpine foliation (0.4–0.5 GPa; Guntli and Liniger, 1989). The growth of thin garnet rims in equilibrium with phengite and chlorite from the main foliation suggests heating during decompression (Fig. 7), since garnet commonly requires temperatures >450 °C to form. This event may relate with the D2 postpeak stage reported by Handy et al. (1996) and referred as "T-dominated" in Villa et al. (2000). We emphasize that some uncertainty exists on P-T estimates for the burial P-T conditions (at least several tens of degrees and possibly a few hundred MPa) due to their strong dependence on phengite solid solution model (and associated Si isopleths) as well as the control of MnO concentration on the "Garnet-in" reaction location (e.g., Mahar et al., 1997).

Interpretation of Age Data

Calculating the Rb/Sr isochron for white micas from metasediments marking the boundaries between the crystalline nappes yielded an age of 48.9 ± 0.9 Ma. Since there is no correlation between mica grain size and apparent age for this sample, we consider this a robust age. Moreover, it is identical to the age obtained by Bachmann et al. (2009b) for the youngest movements at the plate interface farther north in southern Switzerland and relatively close to the ages obtained by Picazo et al. (2019). It has been particularly difficult to derive meaningful age information for the crystalline basement rocks, since the various mineral fractions separated reveal significant disequilibrium, including the low-Rb/Sr phases such as apatite, albite, or titanite. Large mica grains seem apparently older than younger grains, which is a characteristic signature for incomplete recrystallization (Figs. 8B and 8C). We interpret the Sr disequilibrium and the obvious evidence for much older isotopic signatures as an incomplete overprint of possibly Variscan ages during Alpine shearing. An analogous conclusion has been already drawn for similar rocks from the base of the Austroalpine nappe farther north (Bachmann et al., 2009b) and west in the Dent Blanche Massif (Angiboust et al., 2014).

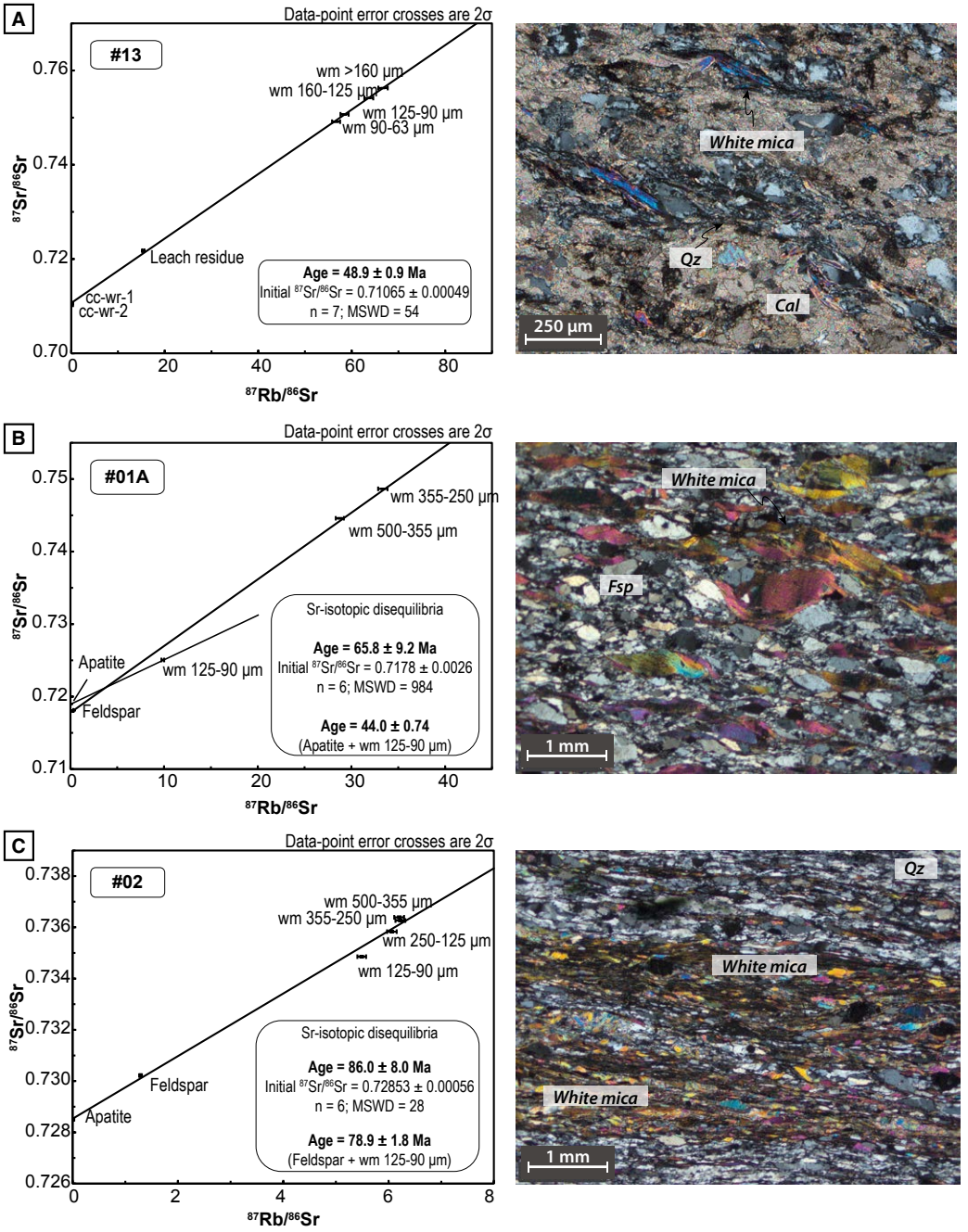

Figure 8. Rb/Sr mineral data (left column) and characteristic rock fabrics under optical microscope (right column) for three samples. (A) Sample #13 from Permo-Mesozoic metasediments. (B) Sample #01A. (C) Sample #02; B and C from the Margna nappe. Analytical data are given in Supplemental Item S2 (text footnote 1). Grain size is indicated because different grain-size fractions were analyzed.

TABLE 3. FULL RESULTS OF WHITE MICA $^{40}Ar/^{39}Ar$ STEPWISE-HEATING ANALYSIS

Run ID	$^{40}Ar/^{39}Ar$ (±1σ)	$^{38}Ar/^{39}Ar$ (±1σ)	$^{37}Ar/^{39}Ar$ (±1σ)	$^{36}Ar/^{39}Ar$ (10^{-3} ±1σ)	$^{40}Ar^*$ (%)	$^{39}Ar^*$ (%)	$^{40}Ar^*/^{39}Ar$ (±1σ)	Age (Ma)	±1σ
01A-H									
1043-01	164.819 ± 4.718	0.157 ± 0.018	1.841 ± 0.685	449.936 ± 14.033	19.4	0.4	32.046 ± 2.250	56.7	3.9
1043-02	51.087 ± 0.852	0.036 ± 0.004	0.844 ± 0.217	53.965 ± 2.002	68.9	1.3	35.223 ± 0.867	62.3	1.5
1043-03	42.588 ± 0.285	0.016 ± 0.001	0.000 ± 0.024	6.178 ± 1.345	95.7	4.6	40.755 ± 0.487	71.9	0.8
1043-04	38.898 ± 0.154	0.015 ± 0.001	0.000 ± 0.016	4.339 ± 0.118	96.7	7.6	37.608 ± 0.155	66.4	0.3
1043-05	38.859 ± 0.120	0.013 ± 0.001	0.001 ± 0.014	3.421 ± 0.097	97.4	9.4	37.843 ± 0.122	66.8	0.2
1043-06	38.742 ± 0.109	0.013 ± 0.000	0.002 ± 0.010	2.043 ± 0.081	98.4	13.6	38.134 ± 0.111	67.3	0.2
1043-07	37.364 ± 0.096	0.013 ± 0.000	0.012 ± 0.008	1.627 ± 0.061	98.7	18.7	36.879 ± 0.098	65.1	0.2
1043-08	36.824 ± 0.115	0.013 ± 0.000	0.011 ± 0.009	1.170 ± 0.057	99.1	15.2	36.474 ± 0.115	64.4	0.2
1043-09	36.579 ± 0.128	0.013 ± 0.001	0.000 ± 0.014	0.939 ± 0.097	99.2	10.8	36.295 ± 0.131	64.1	0.2
1043-10	34.711 ± 0.119	0.012 ± 0.000	0.000 ± 0.014	1.428 ± 0.115	98.8	9.2	34.283 ± 0.124	60.6	0.2
1043-11	46.318 ± 2.641	0.019 ± 0.001	0.065 ± 0.026	3.020 ± 0.257	98.1	5.0	45.428 ± 2.591	79.9	4.5
1043-12	40.014 ± 0.204	0.013 ± 0.000	0.049 ± 0.036	3.029 ± 0.219	97.8	4.2	39.119 ± 0.212	69.0	0.4
01A-L									
1042-01	224.501 ± 3.376	0.133 ± 0.004	0.126 ± 0.156	587.686 ± 9.082	22.6	0.4	50.849 ± 1.572	88.4	2.7
1042-02	51.076 ± 0.321	0.023 ± 0.001	0.084 ± 0.030	48.325 ± 0.590	72.1	1.5	36.800 ± 0.305	64.4	0.5
1042-03	44.919 ± 0.172	0.018 ± 0.001	0.020 ± 0.013	26.888 ± 0.231	82.3	4.0	36.971 ± 0.169	64.7	0.3
1042-04	39.601 ± 0.186	0.014 ± 0.000	0.007 ± 0.020	8.049 ± 0.134	94.0	4.7	37.218 ± 0.181	65.1	0.3
1042-05	38.325 ± 0.112	0.014 ± 0.000	0.000 ± 0.013	5.153 ± 0.100	96.0	6.8	36.796 ± 0.114	64.4	0.2
1042-06	37.706 ± 0.091	0.013 ± 0.000	0.016 ± 0.009	2.668 ± 0.064	97.9	9.9	36.914 ± 0.092	64.6	0.2
1042-07	37.394 ± 0.112	0.012 ± 0.000	0.000 ± 0.006	2.391 ± 0.050	98.1	12.8	36.682 ± 0.112	64.2	0.2
1042-08	37.836 ± 0.122	0.012 ± 0.000	0.000 ± 0.005	2.595 ± 0.048	98.0	14.2	37.063 ± 0.122	64.9	0.2
1042-09	36.498 ± 0.140	0.012 ± 0.000	0.000 ± 0.005	1.893 ± 0.056	98.5	13.2	35.934 ± 0.140	62.9	0.2
1042-10	36.535 ± 0.127	0.013 ± 0.001	0.012 ± 0.012	1.301 ± 0.069	99.0	8.8	36.146 ± 0.128	63.3	0.2
1042-11	37.631 ± 0.122	0.013 ± 0.000	0.000 ± 0.008	1.312 ± 0.088	99.0	6.7	37.236 ± 0.124	65.2	0.2
1042-12	37.816 ± 0.152	0.017 ± 0.001	0.000 ± 0.019	1.127 ± 0.173	99.1	3.9	37.477 ± 0.160	65.6	0.3
1042-13	37.010 ± 0.138	0.012 ± 0.000	0.026 ± 0.009	1.508 ± 0.055	98.8	13.2	36.562 ± 0.138	64.0	0.2
01A-P									
1035-01	297.763 ± 3.950	0.167 ± 0.003	0.120 ± 0.127	747.150 ± 10.311	25.9	0.8	76.991 ± 1.820	132.0	3.0
1035-02	79.382 ± 0.893	0.029 ± 0.005	0.052 ± 0.085	136.867 ± 1.806	49.1	1.4	38.938 ± 0.649	68.1	1.1
1035-03	58.068 ± 0.570	0.035 ± 0.002	0.054 ± 0.054	79.440 ± 1.083	59.6	2.0	34.594 ± 0.468	60.6	0.8
1035-04	48.525 ± 0.310	0.023 ± 0.001	0.084 ± 0.036	52.819 ± 0.565	67.8	3.7	32.920 ± 0.284	57.7	0.5
1035-05	35.954 ± 0.164	0.016 ± 0.001	0.028 ± 0.019	9.110 ± 0.187	92.5	7.3	33.259 ± 0.165	58.3	0.3
1035-06	35.620 ± 0.187	0.016 ± 0.001	0.036 ± 0.018	6.987 ± 0.196	94.2	7.6	33.554 ± 0.189	58.8	0.3
1035-07	34.939 ± 0.151	0.013 ± 0.001	0.000 ± 0.011	3.316 ± 0.111	97.2	14.4	33.954 ± 0.153	59.5	0.3
1035-08	35.565 ± 0.091	0.013 ± 0.000	0.000 ± 0.009	2.259 ± 0.073	98.1	21.8	34.893 ± 0.093	61.1	0.2
1035-09	34.875 ± 0.119	0.013 ± 0.001	0.000 ± 0.015	3.083 ± 0.138	97.4	10.0	33.958 ± 0.124	59.5	0.2
1035-10	33.033 ± 0.155	0.014 ± 0.000	0.001 ± 0.014	4.650 ± 0.146	95.8	8.9	31.654 ± 0.156	55.5	0.3
1035-11	33.844 ± 0.174	0.012 ± 0.001	0.040 ± 0.016	3.700 ± 0.199	96.8	7.0	32.750 ± 0.180	57.4	0.3
1035-12	34.386 ± 0.219	0.013 ± 0.001	0.006 ± 0.034	3.582 ± 0.434	96.9	3.1	33.323 ± 0.249	58.4	0.4
1035-13	45.331 ± 0.407	0.014 ± 0.001	0.000 ± 0.083	3.855 ± 0.970	97.5	1.3	44.180 ± 0.491	77.0	0.8
1035-14	41.862 ± 0.167	0.014 ± 0.001	0.362 ± 0.016	6.736 ± 0.142	95.3	10.7	39.905 ± 0.168	69.7	0.3

TABLE 4. FULL RESULTS OF WHITE MICA $^{40}Ar/^{39}Ar$ IN-SITU UV LASER PROBE ANALYSIS

Run ID	$^{40}Ar/^{39}Ar$ (±1σ)	$^{38}Ar/^{39}Ar$ (±1σ)	$^{37}Ar/^{39}Ar$ (±1σ)	$^{36}Ar/^{39}Ar$ (10^{-3} ±1σ)	$^{40}Ar^*$ (%)	$^{40}Ar^*/^{39}Ar$ (±1σ)	Age (Ma)	± 1σ
S-planes								
1049-09	60.786 ± 1.149	0.023 ± 0.005	0.000 ± 0.666	71.470 ± 4.470	65.1	39.503 ± 1.558	70.7	2.7
1049-10	86.312 ± 2.446	0.061 ± 0.011	0.028 ± 1.412	126.557 ± 8.745	56.7	48.912 ± 2.943	87.2	5.1
1049-12	74.229 ± 2.317	0.000 ± 0.0127	0.000 ± 1.373	10.467 ± 1.035	58.0	42.956 ± 3.411	76.8	6.0
1049-20	40.893 ± 0.772	0.024 ± 0.005	0.104 ± 0.646	55.916 ± 3.776	59.6	24.375 ± 1.281	44.0	2.3
1049-21	37.481 ± 0.710	0.022 ± 0.004	0.533 ± 0.557	23.640 ± 2.737	81.5	30.544 ± 1.034	54.9	1.8
1049-23	35.848 ± 0.617	0.023 ± 0.002	0.316 ± 0.448	24.323 ± 3.723	80.0	28.687 ± 1.227	51.6	2.2
1049-24	40.354 ± 0.543	0.025 ± 0.002	0.262 ± 0.359	23.795 ± 2.909	82.6	33.344 ± 0.991	59.9	1.8
1049-26	33.450 ± 0.417	0.017 ± 0.002	0.002 ± 0.278	2.523 ± 1.407	97.8	32.699 ± 0.587	58.7	1.0
1049-28	34.225 ± 0.336	0.018 ± 0.002	0.081 ± 0.204	1.774 ± 1.185	98.5	33.704 ± 0.484	60.5	0.9
C-planes								
1049-11	50.722 ± 1.119	0.008 ± 0.005	0.000 ± 0.788	38.901 ± 4.845	77.2	39.147 ± 1.713	70.1	3.0
1049-16	36.612 ± 0.815	0.019 ± 0.006	0.039 ± 0.527	7.753 ± 4.644	93.8	34.320 ± 1.581	61.6	2.8
1049-19	39.028 ± 0.543	0.021 ± 0.003	0.000 ± 0.277	26.518 ± 1.705	79.9	31.179 ± 0.686	56.0	1.2
1049-29	36.245 ± 0.589	0.017 ± 0.003	0.000 ± 0.332	0.000 ± 2.132	102.0	36.960 ± 0.868	66.2	1.5

To test whether the K-Ar system of white mica was more equilibrated than Rb/Sr in the crystalline basement rocks and to potentially avoid the problem of contamination of the Alpine signal by pre-Alpine isotopic relics, we analyzed white micas derived from one mylonitic gneiss from Margna and one foliated cataclasite from Sella, by $^{40}Ar/^{39}Ar$ stepwise heating and in situ dating, respectively. We analyzed the samples with the least fraction of isotopic relics. This approach enabled the production of age data from regions of the samples most pervasively affected by mylonitization. Microscopically, the sample used for stepwise-heating dating did not exhibit core-rim structures in phengite crystals. Three mica fractions were dated, yielding an age of 61.1–66.2 ± 0.3 Ma, and a plateau age of 64.6 ± 0.3 Ma was calculated for one of the fractions. In situ $^{40}Ar/^{39}Ar$ age results for sample #18D (foliated cataclasite), however, yielded a large span of ages from 44.0 to 70.7 Ma (see Fig. 10G). Neither an apparent systematic relation was observed between S- and C-structures and their calculated ages nor a correlation of the two structures with different Si content (Fig. 6B; unlike for Agard et al., 2002).

It is known that extraneous ^{40}Ar (including both excess and inherited argon) can be commonly found in HP and UHP basement rocks (Scaillet, 1996; Sherlock and Kelley, 2002; Di Vincenzo et al., 2006, and references therein) and that in its presence apparently older and meaningless geological ages can be obtained. Excess argon might be present due to diffusion through grain boundaries, whereas inherited argon can result from preexisting argon from older minerals whose isotopic signature did not get fully re-equilibrated by the metamorphic imprint that one aims to date.

In the present study, the mylonitic sample dated with $^{40}Ar/^{39}Ar$ stepwise heating (#01A) exhibits disequilibrium of its isotopic signature, as attested by the lack of plateau for two mica fractions and the different ages calculated for different mica fractions, especially since bigger fractions (#01A-P) yield younger ages than the finer ones (compare Fig. 9C with Figs. 9A and 9B). Furthermore, ages obtained by in situ dating on the foliated cataclasite (#18D) exhibit a wide range of values (44–87 Ma; Fig. 10G), which, however, fall within the range of published Alpine deformation ages in the Central Alps in general (K-Ar on phengite crystals, Handy et al., 1996; $^{40}Ar/^{39}Ar$ on amphiboles, Villa et al., 2000; Fig. 3), as well as for the time window of active subduction as inferred from the spread of pseudotachylyte ages (Bachmann et al., 2009b) along the same contact. The aforementioned geochronological heterogeneities are also reflected in the petrochemical signature of the rocks: feldspar boudins, mica fish within recrystallized mica fibers (Fig. 5A), and multiple phengite generations (Figs. 6A and 6B). Based on the above heterogeneities and our previous interpretation of the age data as indicative of maximum ages for the cessation of deformation, we cannot exclude the presence of extraneous ^{40}Ar in our samples.

As already mentioned, the maximum Rb/Sr ages for the end of Alpine deformation (44.0 and 54.3 Ma) coincide with the youngest in situ $^{40}Ar/^{39}Ar$ ages (44.0 Ma; see Table 5). We interpret the older ages obtained as reflecting mixed ages, due to incomplete recrystallization and only partial isotopic resetting, while we interpret the youngest ones as maximum age for the end of deformation (see also Fig. 10H and Picazo et al., 2019). Finally, we emphasize that the seeming discrepancy with the studies of Handy et al. (1996) and Mohn et al. (2011) is due to the terminology used and not to the processes themselves: what these authors refer to as collision/D3 deformation is considered in our study a stage of "subduction of continental Austroalpine sliver(s)."

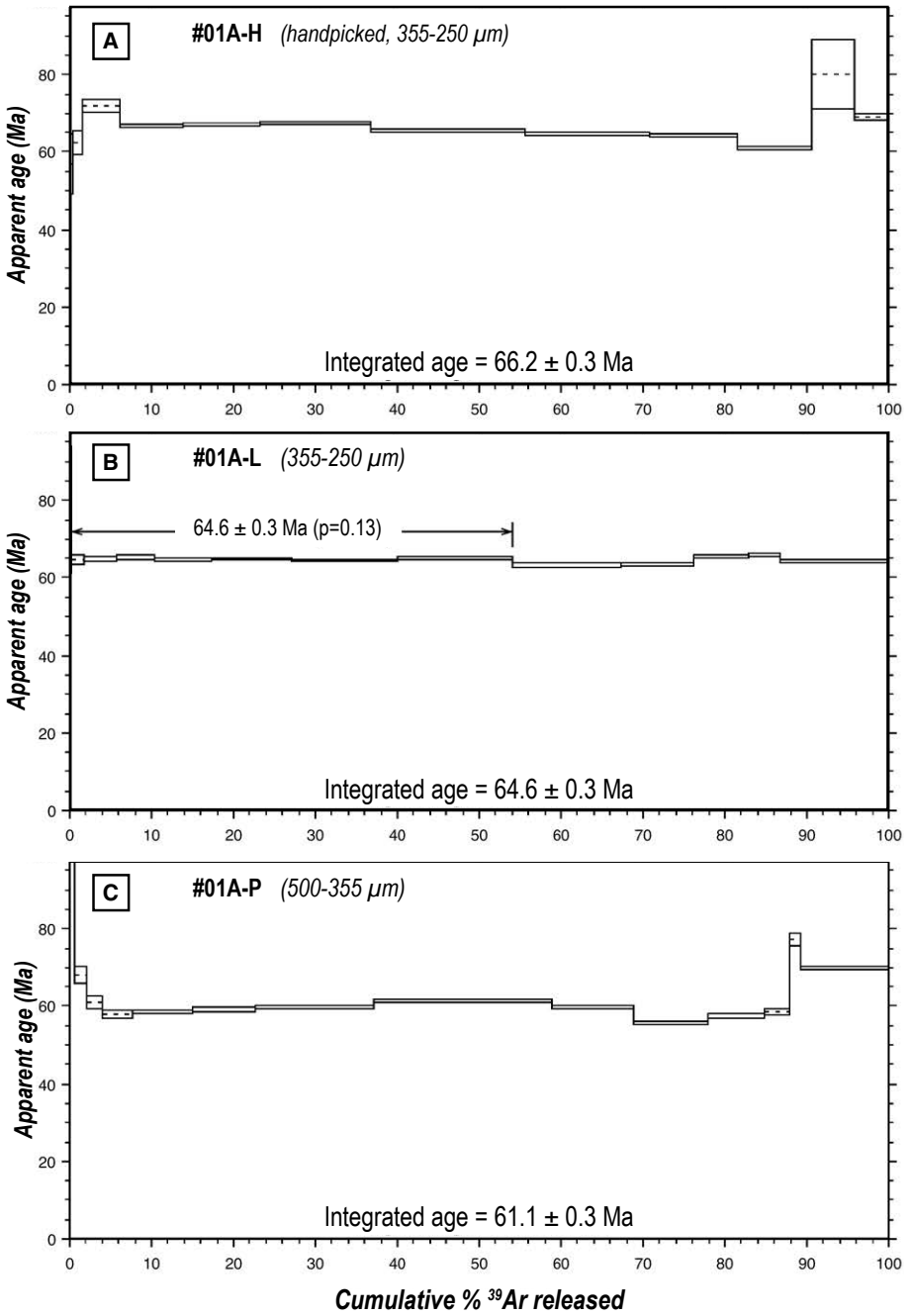

Figure 9. White mica $^{40}Ar/^{39}Ar$ age spectra obtained for sample #01A by stepwise- heating experiments. Total gas ages were determined by integrating over all steps. Steps attributed to the plateau are highlighted in black. Uncertainties are given in 2σ; H—handpicked fractions of 355–250 µm; L—fractions of (355–250 µm) obtained by the "tapping or shaking paper" method; P—fractions of (500–355 µm) obtained by the same method as L.

Alpine Deformation along the Base of the Austroalpine Stack

The base of the Austroalpine nappes in Central and Western Alps (Dent Blanche) has been proposed by Bachmann et al. (2009b) and Angiboust et al. (2015), respectively, as a field analogue for the roof of an ancient subduction interface (see also Froitzheim and Manatschal, 1996; Froitzheim et al.,1996; Schmid et al., 2004 for paleogeographic reconstructions). Although the presence of a metamorphic gradient along the Arosa–St. Moritz–Malenco transect is well known (e.g., Trommsdorff, 1983; Guntli and Liniger, 1989), up to now this part of the Austroalpine-Penninic boundary has not been studied in the frame of the subduction interface.

The Val Malenco setting is a plate interface zone characterized by abundant underplated continental slivers (such as the Sella and Margna nappes), which likely represent extensional allochthons of the Apulian upper plate, sheared off early in the subduction history and transported toward depth. Hence, the Margna and Intra-Sella shear zones (MSZ and ISSZ, respectively) correspond to parts of a shear zone network forming the plate interface zone in their entirety. As suggested by Beltrando et al. (2010) and Mohn et al. (2011), it is conceivable, but not easily tested, that preexisting extensional faults, active during Jurassic rifting, could have facilitated the detachment from the downgoing slab during the subduction event.

The shear zones studied here were, at least kinematically, at one point in their lifetime part of the plate interface shear-zone network. Since these shear zones are interface-parallel and none of them ends blindly high up (nor crosses the units at an angle), we exclude the possibility that they represent splay faults into the upper plate. We rather assume that they formed part of a network

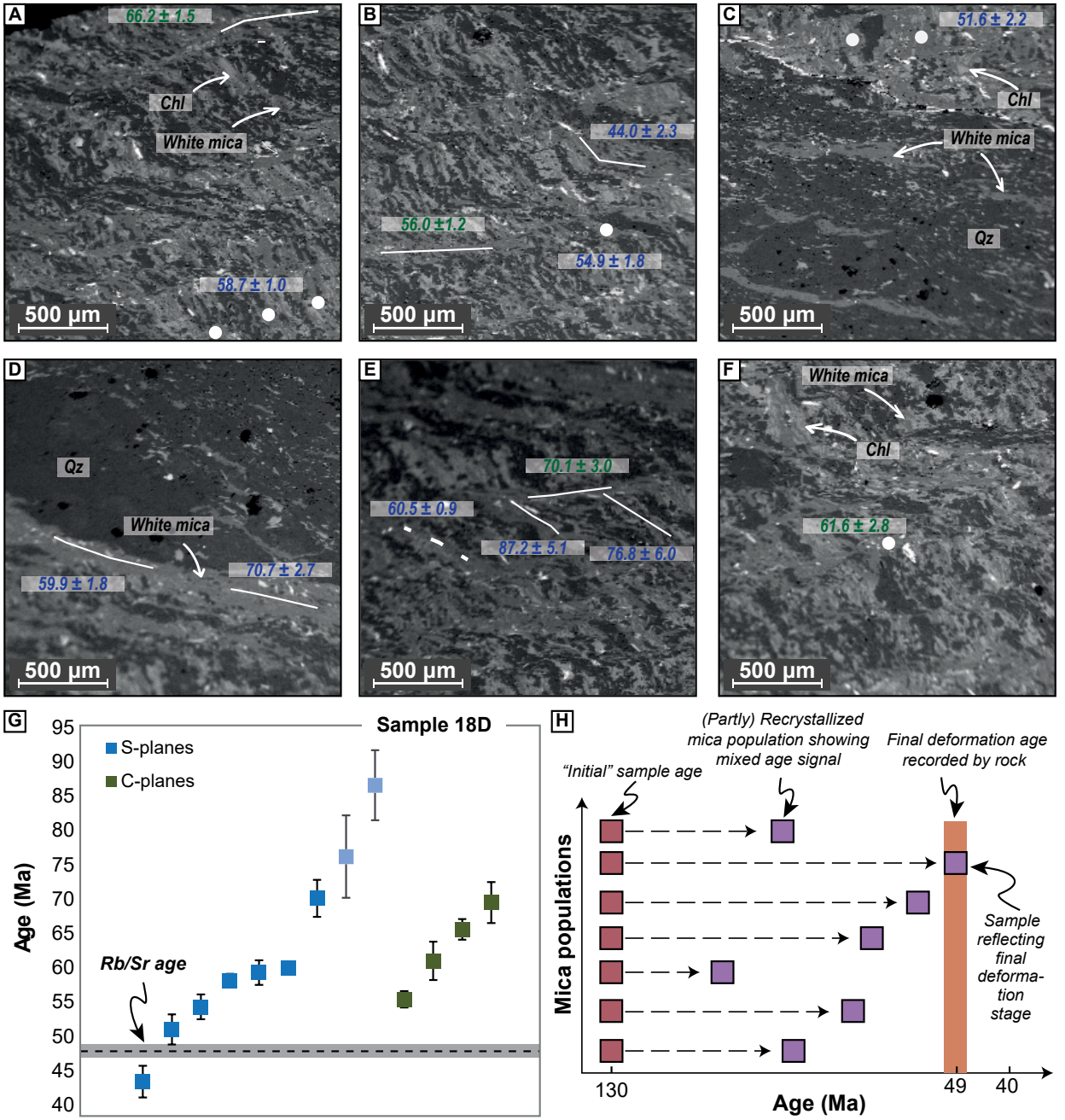

Figure 10. (A–F) Scanning electron microscope (SEM) backscattered electron photomicrographs of studied white mica–bearing sample #18D and the location of the analyzed domains during laser ablation in white micas; blue colors correspond to analyses of S-planes in micas, green colors to C-planes. (G) Summary of apparent ages obtained on white mica by in situ laser analyses; the two transparent age points correspond to measurements with large analytical uncertainty (>5 Ma), which are not taken into consideration for the interpretation of the in situ age data; dashed line corresponds to the age obtained by Rb/Sr on metasediments, and shaded area shows uncertainty at 2σ level. Uncertainties of $^{40}Ar/^{39}Ar$ analyses are given in 1σ. (H) Interpretation of a hypothetical span of both Rb/Sr and $^{40}Ar/^{39}Ar$ measurements; *x*-axis shows age (Ma), *y*-axis the different mica populations dated. The older ages (red squares) would correspond either to age of formation of the rock or complete pre-Alpine deformation. Full isotope resetting and re-equilibration of the rock would give ages clearly clustered around the last event of deformation (orange bar, e.g., at ca. 49 Ma). A geochronological signal similar to the purple squares, namely scattered deformation ages, would reflect mixed ages due to incomplete recrystallization and/or only partial isotopic resetting. The youngest age can, therefore, only be interpreted as the maximum age for the end of deformation.

TABLE 5. OVERVIEW OF AGE DATA ACQUIRED IN THIS STUDY

Sample	Rb/Sr age (Ma)	Ar/Ar age (Ma)	Interpretation
Margna			
#01A	44	61–66 (stepwise)	Rb/Sr maximum age for end of deformation
#01F	54	n/a	Same as above
#02	Disequilibria	n/a	Rb/Sr disequilibria
Sella			
#18D	n/a	44–87 (in situ)	Age span covering most of P-dominated Alpine deformation
#23B	Disequilibria	n/a	Rb/Sr disequilibria
Metasediments			
#13	48.9 ± 0.9	n/a	Synkinematic metamorphic (re)crystallization: deformation age

n/a—not applicable.

belonging to the plate interface as long as they were active. This would make the system kinematically similar to the finding by Angiboust et al. (2014) on the evolution and stacking of interfaces through progressive underplating of duplex units. Unfortunately, our dating results do not resolve whether they were sequentially active—as in the Dent Blanche area—or active simultaneously. We stress that exhumation and collision have left an imprint in the present-day structures. However, our sampling and observations were limited to areas with minimum reworking, as shown by the white mica zoning pattern, which exhibits only minor exhumation-related zoning and by the moderate back-shearing observed in the kinematic indicators along main thrust contacts. In addition, the youngest ages near 44 Ma that we obtained are older than the late Eocene–Oligocene collisional event that started at ca. 40 Ma and continued until ca. 25 Ma (e.g., Becker, 1993; Markley et al.; 1998, Price et al., 2018) related to the entrance of the European continental margin in the Alpine subduction zone and associated with a kinematic inversion of subduction-related structures.

Despite some uncertainties due to the scarcity of pressure indicators, our estimates plot deeper than for Arosa and St. Moritz, for which peak burial temperatures of 200°–250 °C and 300°–350 °C have been estimated, respectively (Fig. 7; Bachmann et al., 2009b). On a microstructural point of view, the Alpine deformation and the associated mylonitic deformation are much more extensively expressed in the Malenco region than along shallower equivalents (see fabric description from Bachmann et al., 2009a, 2009b; Fig. 11). In fact, large mylonitic corridors are commonly observed in Margna and Sella nappes, unlike Arosa and St. Moritz, where deformation of the Austroalpine units is mostly expressed by microscale fractures in shallower parts and recrystallization of sheet silicates deeper. The larger amount of ductile imprint is likely a consequence of increasingly higher peak burial temperatures from Arosa, through Malenco down to Dent Blanche regions at also slower strain rates. Veining and mineralization within the Austroalpine units of the study area are not pervasive, which agrees with observations for the shallower basal parts of the Austroalpine, in the Arosa–St. Moritz region (Bachmann et al., 2009b).

One of the main differences between Arosa–St. Moritz and Malenco is the absence of in situ pseudotachylytes along the base of the Austroalpine units of the latter. In the study area of Bachmann et al. (2009b), pseudotachylytes are abundant in the northern part of the transect, providing evidence for high strain rates at seismic slip velocities; the southernmost (and hence deepest) locality where pseudotachylytes along the plate interface zone are mentioned is SW of St. Moritz, where peak temperatures of ~350 °C were reached. In our study area, a significant number of pseudotachylytes was observed only in the form of fallen blocks along streams; but based on their abundance and location in which they were found, we hypothesize they derive from the hanging wall, i.e., higher Austroalpine units, such as Upper Sella and/or Bernina nappes (Fig. 4l). The rocks studied in the Val Malenco region accommodated shearing predominantly by ductile flow with limited cataclastic networks (Fig. 11). While this observation, along with the evidence for repeated hydrofracturing, is indicative of variations in creep velocity by at least several orders of magnitude, there is no clear evidence as to whether they are related to slip at seismic velocities, i.e., at 1 m/s. Along the base of the Dent Blanche basal thrust, the close genetic link between foliated cataclasites with metamorphic veins led Angiboust et al. (2015) to propose their association with semi-brittle and brittle-ductile switches, potentially the record of transient slow slip events that take place near the base of the seismogenic zone. Some pseudotachylytes found in the core of Dent Blanche Massif (Valpelline unit) were interpreted as the consequences of the accumulation of high stresses in very stiff rocks that were not prone to breaking (Menant et al., 2018). Their age is coeval with peak burial conditions, pointing to heterogeneous deformation patterns at depth in accreted continental slivers in the Alpine channel. They may or may not be coeval with the pseudotachylytes found as fallen blocks in our study area. It has yet to be shown whether the Bernina pseudotachylytes formed during the

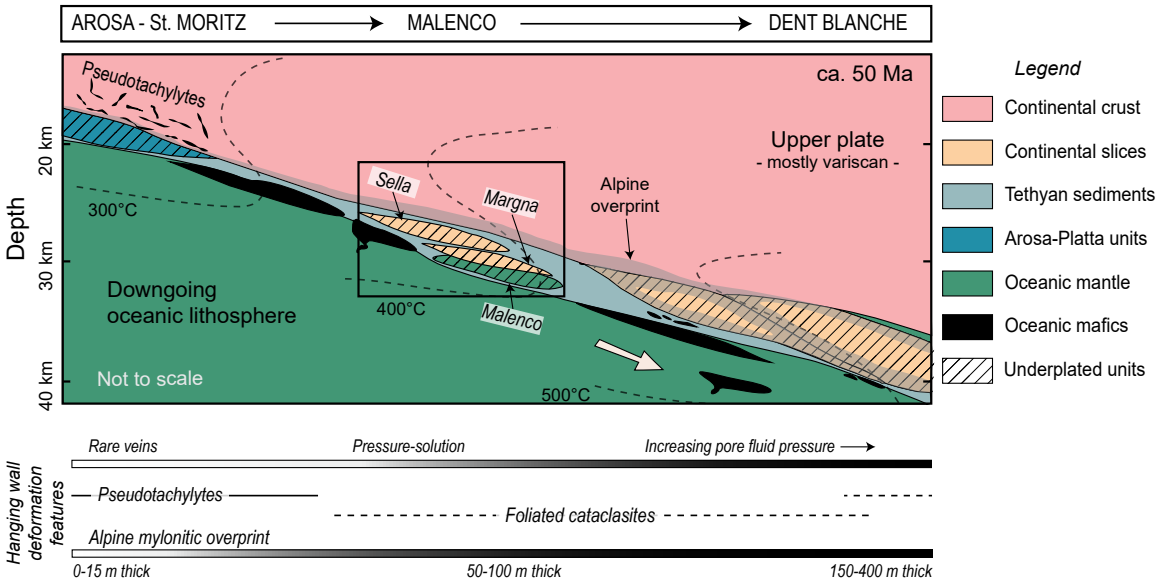

Figure 11. Synthetic sketch summarizing the structure of the paleo-Alpine interface at ca. 50 Ma, when Margna and Sella nappes were already basally accreted to the Austroalpine tectonic edifice. Val Malenco deformation patterns are compared in this figure with features reported by Bachmann et al. (2009a, 2009b) for the shallower region and by Angiboust et al. (2014) and Menant et al. (2018) for the deeper regions.

rifting phase (e.g., Bissig and Hermann, 1999; Mohn et al., 2011), or if they formed in a similar manner as for the Valpelline unit in the Dent Blanche Massif. With the absence of distinct fabrics that may be related to seismogenic deformation and temperatures of ~400 °C, we, therefore, hypothesize that this part of the Alpine subduction zone represents the deformation styles of the transition zone, found globally to characterize the downdip end of seismicity toward aseismic creep at similar temperatures (e.g., Hyndman et al., 1997; Oleskevich et al., 1999). Moreover, the findings corroborate repeated switches between slower and faster creep velocities and near-lithostatic pore-fluid pressure conditions characterizing this depth domain, similar to findings in this depth region found instrumentally in many active subduction settings.

CONCLUSIONS

The Lower Austroalpine units in the Malenco region were subducted, underplated, and partly re-crystallized during the long history of Alpine convergence. The dominant deformation pattern along Alpine shear zones affecting the Austroalpine bodies during peak burial (at ~400 °C and 0.9 GPa) is ductile with widespread pressure-solution as well as local semi-brittle (fractured albite) and brittle, cataclastic networks. Rb/Sr geochronology on mica-rich metasediments deposited during Jurassic rifting and later metamorphosed during Alpine convergence yields a robust age of deformation and (re)crystallization of 48.9 ± 0.9 Ma. However, our Rb/Sr as well as $^{40}Ar/^{39}Ar$ dating of some Alpine, seemingly recrystallized white micas from mylonites and one foliated cataclasite of the crystalline basement reveal a wide range of ages, which, despite falling within the range obtained by previous studies (Handy et al., 1996; Villa et al., 2000; Picazo et al., 2019), can only be considered as mixed ages due to partial resetting of the isotopic signature of the system.

Putting together recent findings in the broader Val Malenco area (e.g., Droop and Chavrit, 2014; Picazo et al., 2019) and the P-T-t results of this study, we highlight the existence, during the geodynamic evolution of the Central Alps, of a continuous subduction and underplating process along the active subduction interface, from the upper nappes (Austroalpine) toward the deeper ones (Malenco). The Val Malenco area sheds light onto a region below the seismogenic depths exposed in Arosa–St. Moritz and displays subduction-related deformation at a depth range in the transition zone, which is globally found to host both slow creep as well as more rapid silent slip events.

ACKNOWLEDGMENTS

This research was funded by the People Programme (Marie Curie Actions) of the European Union's Seventh Framework Programme FP7/2017–2013/under REA grant agreement no. 604713, "Zooming in between Plates (ZIP)" and by a USPC-IDEX grant to S.A. O. Müntener is acknowledged for fruitful scientific discussion. C. Pranger and S. Olivotos are thanked for assistance during fieldwork and M. Locatelli for useful discussions. M. Dziggel is also acknowledged for helping with the digitization of the geological map. We thank U. Ring, an anonymous reviewer, and Guest Associate Editor G. Bebout for their constructive reviews. This is Institut de Physique du Globe de Paris (IPGP) contribution #4094.

REFERENCES CITED

Agard, P., Vidal, O., and Goffé, B., 2001, Interlayer and Si content of phengites in high-pressure carpholite-bearing metapelites: Journal of Metamorphic Geology, v. 19, p. 479–495, https://doi.org/10.1046/j.0263-4929.2001.00322.x.

Agard, P., Monié, P., Jolivet, L., and Goffé, B., 2002, Exhumation of the Schistes Lustrés complex: In situ laser probe $^{40}Ar/^{39}Ar$ constraints and implications for the Western Alps: Journal of Metamorphic Geology, v. 20, p. 599–618, https://doi.org/10.1046/j.1525-1314.2002.00391.x.

Agard, P., Plunder, A., Angiboust, S., Bonnet, G., and Ruh, J., 2018, The subduction plate interface: Rock record and mechanical coupling (from long to short timescales): Lithos, v. 320–321, p. 537–566, https://doi.org/10.1016/j.lithos.2018.09.029.

Angiboust, S., Glodny, J., Oncken, O., and Chopin, C., 2014, In search of transient subduction interfaces in the Dent Blanche–Sesia Tectonic system (W. Alps): Lithos, v. 205, p. 298–321, https://doi.org/10.1016/j.lithos.2014.07.001.

Angiboust, S., Kirsch, J., Oncken, O., Glodny, J., Monié, P., and Rybacki, E., 2015, Probing the transition between seismically coupled and decoupled segments along an ancient subduction interface: Geochemistry, Geophysics, Geosystems, v. 16, p. 1905–1922, https://doi.org/10.1002/2015GC005776.

Babist, J., Handy, M.R., Konrad-Schmolke, M., and Hammerschmidt, K., 2006, Precollisional, multistage exhumation of subducted continental crust: The Sesia Zone, western Alps: Tectonics, v. 25, https://doi.org/10.1029/2005TC001927.

Bachmann, R., Glodny, J., Oncken, O., and Seifert, W., 2009a, Abandonment of the South Penninic-Austroalpine palaeosubduction zone, Central Alps, and shift from subduction erosion to accretion: Constraints from Rb/Sr geochronology: Journal of the Geological Society of London, v. 166, p. 217–231, https://doi.org/10.1144/0016-76492008-024.

Bachmann, R., Oncken, O., Glodny, J., Seifert, W., Georgieva, V., and Sudo, M., 2009b, Exposed plate interface in the European Alps reveals fabric styles and gradients related to an ancient seismogenic coupling zone: Journal of Geophysical Research. Solid Earth, v. 114, p. 1–23, https://doi.org/10.1029/2008JB005927.

Becker, H., 1993, Garnet peridotite and eclogite Sm-Nd mineral ages from the Lepontine dome (Swiss Alps): New evidence for Eocene high-pressure metamorphism in the central Alps: Geology, v. 21, p. 599–602, https://doi.org/10.1130/0091-7613(1993)021<0599:GPAESN>2.3.CO;2.

Beltrando, M., Compagnoni, R., and Lombardo, B., 2010, (Ultra-) High-pressure metamorphism and orogenesis: An Alpine perspective: Gondwana Research, v. 18, p. 147–166, https://doi.org/10.1016/j.gr.2010.01.009.

Bissig, T., and Hermann, J., 1999, From pre-Alpine extension to Alpine convergence: The example of the southwestern margin of the Margna nappe (Val Malenco, N-Italy): Schweizerische Mineralogische und Petrographische Mitteilungen, v. 79, p. 363–380.

Cliff, R.A., and Meffan-Main, S., 2003, Evidence from Rb-Sr microsampling geochronology for the timing of Alpine deformation in the Sonnblick Dome, SE Tauern Window, Austria: Geological Society of London, Special Publications, v. 220, p. 159–172, https://doi.org/10.1144/GSL.SP.2003.220.01.09.

Compagnoni, R., Dal Piaz, G.V., Hunziker, J.C., Gosso, G., Lombardo, B., and Williams, P.F., 1977, The Sesia-Lanzo zone, a slice of continental crust with alpine high pressure-low temperature assemblages in the Western Italian Alps: Rendiconti della Società Italiana di Mineralogia e Petrologia, v. 33, p. 281–334.

Connolly, J.A., 2005, Computation of phase equilibria by linear programming: A tool for geodynamic modeling and its application to subduction zone decarbonation: Earth and Planetary Science Letters, v. 236, p. 524–541, https://doi.org/10.1016/j.epsl.2005.04.033.

Conrad, C.P., Bilek, S., and Lithgow-Bertelloni, C., 2004, Great earthquakes and slab pull: Interaction between seismic coupling and plate-slab coupling: Earth and Planetary Science Letters, v. 218, p. 109–122, https://doi.org/10.1016/S0012-821X(03)00643-5.

Dal Piaz, G.V., Bistacchi, A., and Massironi, M., 2003, Geological outline of the Alps: Episodes, v. 26, p. 175–180, https://doi.org/10.18814/epiiugs/2003/v26i3/004.

Deutsch, A., 1983, Datierung an Alkaliamphibolen und Stilpnomelan der südlichen Platta-Decke: Eclogae Geologicae Helvetiae, v. 76, p. 295–308.

Di Vincenzo, G., Rocchi, S., Rossetti, F., and Storti, F., 2006, Dating brittle faulting: Exploiting the complementarity of the step-heating and in situ ^{40}Ar-^{39}Ar laser techniques to solve the complexity of Cenozoic pseudotachylytes from the West Antarctic Rift System: Terra Antarctica Reports, v. 12, p. 49–56.

Droop, G.T., and Chavrit, D., 2014, Eclogitic metagabbro from the Lanzada Window, eastern Central Alps: Confirmation of subduction beneath the Malenco Unit: Swiss Journal of Geosciences, v. 107, p. 113–128, https://doi.org/10.1007/s00015-014-0162-z.

Dürr, S.B., 1992, Structural history of the Arosa Zone between Platta and Err Nappes east of Marmorera (Grisons): Multiphase deformation at the Penninic-Austroalpine plate boundary: Eclogae Geologicae Helvetiae, v. 85, p. 361–374.

Ernst, W.G., and Dal Piaz, G.V., 1978, Mineral parageneses of eclogitic rocks and related mafic schists of the Piemonte ophiolite nappe, Breuil–St. Jacques area, Italian Western Alps: The American Mineralogist, v. 63, p. 621–640.

Ferrario, A., and Montrasio, A., 1976, Manganese ore deposit of Monte del Forno. Its stratigraphy and structural implications: Schweizerische Mineralogische und Petrographische Mitteilungen, v. 56, p. 377–385.

Freeman, S.R., Inger, S., Butler, R.W., and Cliff, R.A., 1997, Dating deformation using Rb-Sr in white mica: Greenschist facies deformation ages from the Entrelor shear zone, Italian Alps: Tectonics, v. 16, p. 57–76, https://doi.org/10.1029/96TC02477.

Freeman, S.R., Butler, R.W., Cliff, R.A., and Rex, D.C., 1998, Direct dating of mylonite evolution: A multi-disciplinary geochronological study from the Moine Thrust Zone, NW Scotland: Journal of the Geological Society of London, v. 155, p. 745–758, https://doi.org/10.1144/gsjgs.155.5.0745.

Frey, H., Hunzicker, J.C., Frank, W., Bocquet, J., Dal Piaz, G.V., Jäger, E., and Niggli, E., 1974, Alpine metamorphism of the Alps: A review: Schweizerische Mineralogische und Petrographische Mitteilungen, v. 54, p. 247–290.

Froitzheim, N., and Manatschal, G., 1996, Kinematics of Jurassic rifting, mantle exhumation, and passive-margin formation in the Austroalpine and Penninic nappes (eastern Switzerland): Geological Society of America Bulletin, v. 108, p. 1120–1133, https://doi.org/10.1130/0016-7606(1996)108<1120:KOJRME>2.3.CO;2.

Froitzheim, N., Schmid, S.M., and Frey, M., 1996, Mesozoic paleogeography and the timing of eclogite-facies metamorphism in the Alps: A working hypothesis: Eclogae Geologicae Helvetiae, v. 89, p. 81–110, https://doi.org/10.5169/seals-167895.

Fuhrman, M.L., and Lindsley, D.H., 1988, Ternary-feldspar modeling and thermometry: The American Mineralogist, v. 73, p. 201–215, https://doi.org/10.4052/tigg.24.13.

Gautschi, A., 1979, Geologie und Petrologie des Fedozer Gabbros (Östliche Zentralalpen, Prov. Sondrio, N-Italien/Kt. Graubünden, Schweiz): Abstr: Schweizerische Mineralogische und Petrographische Mitteilungen, v. 59, p. 423–427.

Gautschi, A., 1980, Metamorphose und Geochemie der basischen Gesteine des Bergeller Ostrands [Ph.D. thesis]: Zürich, ETH Zürich, 170 p.

Glodny, J., Ring, U., Kühn, A., Gleissner, P., and Franz, G., 2005, Crystallization and very rapid exhumation of the youngest Alpine eclogites (Tauern Window, Eastern Alps) from Rb/Sr mineral assemblage analysis: Contributions to Mineralogy and Petrology, v. 149, p. 699–712, https://doi.org/10.1007/s00410-005-0676-5.

Glodny, J., Ring, U., and Kühn, A., 2008a, Coeval high-pressure metamorphism, thrusting, strike-slip, and extensional shearing in the Tauern Window, Eastern Alps: Tectonics, v. 27, https://doi.org/10.1029/2007TC002193.

Glodny, J., Kühn, A., and Austrheim, H., 2008b, Geochronology of fluid-induced eclogite and amphibolite facies metamorphic reactions in a subduction-collision system, Bergen Arcs, Norway: Contributions to Mineralogy and Petrology, v. 156, p. 27–48, https://doi.org/10.1007/s00410-007-0272-y.

Guntli, P., and Liniger, M., 1989, Metamorphose in der Margna-Decke im Bereich Piz da la Margna und Piz Fedoz (Oberengadin): Schweizerische Mineralogische und Petrographische Mitteilungen, v. 69, p. 289–301.

Halama, R., Konrad-Schmolke, M., Sudo, M., Marschall, H.R., and Wiedenbeck, M., 2014, Effects of fluid-rock interaction on $^{40}Ar/^{39}Ar$ geochronology in high-pressure rocks (Sesia-Lanzo Zone, Western Alps): Geochimica et Cosmochimica Acta, v. 126, p. 475–494, https://doi.org/10.1016/j.gca.2013.10.023.

Handy, M.R., 1996, The transition from passive to active margin tectonics: A case study from the Zone of Samedan (eastern Switzerland): Geologische Rundschau, v. 85, p. 832–851, https://doi.org/10.1007/BF02440114.

Handy, M.R., and Oberhänsli, R., 2004, Explanatory notes to the map: Metamorphic structure of the Alps, age map of the metamorphic structure of the Alps—Tectonic interpretation and outstanding problems: Mitteilungen der Österreichischen Mineralogischen Gesellschaft, v. 149, p. 201–225.

Handy, M.R., Herwegh, M., Kamber, B.S., Tietz, R., and Villa, I.M., 1996, Geochronologic, petrologic and kinematic constraints on the evolution of the Err-Platta boundary, part of a fossil continent-ocean suture in the Alps (eastern Switzerland): Schweizerische Mineralogische und Petrographische Mitteilungen, v. 76, p. 453–474, https://doi.org/10.1145/365696.365701.

Hermann, J., and Müntener, O., 1992, Strukturelle Entwicklung im Grenzbereich zwischen dem penninischen Malenco-Ultramafitit und dem Unterostalpin (Margna- und Sella-Decke): Schweizerische Mineralogische und Petrographische Mitteilungen, v. 72, p. 225–240, https://doi.org/10.5169/seals-54909.

Hermann, J., and Müntener, O., 1996, Extension-related structures in the Malenco-Margna-system: Implications for

paleogeography and consequences for rifting and Alpine tectonics: Schweizerische Mineralogische und Petrographische Mitteilungen, v. 76, p. 501–519.

Hermann, J., Müntener, O., Trommsdorff, V., Hansmann, W., and Piccardo, G.B., 1997, Fossil crust-to-mantle transition, Val Malenco (Italian Alps): Journal of Geophysical Research, v. 102, p. 123–132, https://doi.org/10.1029/97JB01510.

Herrendörfer, R., Van Dinther, Y., Gerya, T., and Dalguer, L.A., 2015, Earthquake supercycle in subduction zones controlled by the width of the seismogenic zone: Nature Geoscience, v. 8, p. 471–474, https://doi.org/10.1038/ngeo2427.

Heuret, A., and Lallemand, S., 2005, Plate motions, slab dynamics and back-arc deformation: Physics of the Earth and Planetary Interiors, v. 149, p. 31–51, https://doi.org/10.1016/j.pepi.2004.08.022.

Holland, T., Baker, J., and Powell, R., 1998, Mixing properties and activity-composition relationships of chlorites in the system MgO-FeO-Al_2O_3-SiO_2-H_2O: European Journal of Mineralogy, v. 10, p. 395–406, https://doi.org/10.1127/ejm/10/3/0395.

Hyndman, R.D., Yamano, M., and Oleskevich, D.A., 1997, The seismogenic zone of subduction thrust faults: The Island Arc, v. 6, p. 244–260, https://doi.org/10.1111/j.1440-1738.1997.tb00175.x.

Inger, S., and Cliff, R.A., 1994, Timing of metamorphism in the Tauern Window, Eastern Alps: Rb-Sr ages and fabric formation: Journal of Metamorphic Geology, v. 12, p. 695–707, https://doi.org/10.1111/j.1525-1314.1994.tb00052.x.

Ishizuka, O., 1998, Vertical and horizontal variations of the fast neutron flux in a single irradiation capsule and their significance in the laser-heating $^{40}Ar/^{39}Ar$ analysis: Case study for the hydraulic rabbit facility of the JMTR reactor, Japan: Geochemical Journal, v. 32, p. 243–252, https://doi.org/10.2343/geochemj.32.243.

Jaeckel, K., Bebout, G.E., and Angiboust, S., 2018, Deformation-enhanced fluid and mass transfer along Western and Central Alps paleo-subduction interfaces: Significance for carbon cycling models: Geosphere, v. 14, p. 2355–2375, https://doi.org/10.1130/GES01587.1.

Kitamura, Y., Sato, K., Ikesawa, E., Ikehara-Ohmori, K., Kimura, G., Kondo, H., Ujiie, K., Onishi, C.T., Kawabata, K., Hashimoto, Y., Mukoyoshi, H., and Masago, H., 2005, Mélange and its seismogenic roof décollement: A plate boundary fault rock in the subduction zone—An example from the Shimanto Belt, Japan: Tectonics, v. 24, https://doi.org/10.1029/2004TC001635.

Konrad-Schmolke, M., Zack, T., O'Brien, P.J., and Barth, M., 2011, Fluid migration above a subducted slab—Thermodynamic and trace element modelling of fluid-rock interaction in partially overprinted eclogite-facies rocks (Sesia Zone, Western Alps): Earth and Planetary Science Letters, v. 311, p. 287–298, https://doi.org/10.1016/j.epsl.2011.09.025.

Liniger, M., 1992, Der ostalpin-penninische Grenzbereich im Gebiet der nördlichen Margna-Decke (Graubünden, Schweiz) [Ph.D. thesis]: Zürich, ETH Zürich, 186 p.

Liniger, M., and Guntli, P., 1988, Bau und Geschichte des zentralen Teils der Margna-Decke: Schweizerische Mineralogische und Petrographische Mitteilungen, v. 68, p. 41–54.

Liniger, M., and Nievergelt, P., 1990, Stockwerk-Tektonik im südlichen Graubünden: Schweizerische Mineralogische und Petrographische Mitteilungen, v. 70, p. 95–101.

Locatelli, M., Verlaguet, A., Agard, P., Federico, L., and Angiboust, S., 2018, Intermediate-depth brecciation along the subduction plate interface (Monviso eclogite, W. Alps): Lithos, v. 320–321, p. 378–402, https://doi.org/10.1016/j.lithos.2018.09.028.

Ludwig, K., 2009, Isoplot v. 3.71: A Geochronological Toolkit for Microsoft Excel: Berkeley, California, Berkeley Geochronology Center, Special Publication no. 4, 70 p.

Mahar, E.M., Baker, J.M., Powell, R., Holland, T.J., and Howell, N., 1997, The effect of Mn on mineral stability in metapelites: Journal of Metamorphic Geology, v. 15, p. 223–238, https://doi.org/10.1111/j.1525-1314.1997.00011.x.

Manatschal, G., 1995, Jurassic rifting and formation of a passive continental margin (Platta and Err nappes, Eastern Switzerland): Geometry, kinematics and geochemistry of fault rocks and a comparison with the Galicia margin [Ph.D. thesis]: Zürich, ETH Zürich.

Markley, M.J., Teyssier, C., Cosca, M.A., Caby, R., Hunziker, J.C., and Sartori, M., 1998, Alpine deformation and $^{40}Ar/^{39}Ar$ geochronology of synkinematic white mica in the Siviez-Mischabel Nappe, western Pennine Alps, Switzerland: Tectonics, v. 17, p. 407–425, https://doi.org/10.1029/98TC00560.

Massonne, H.-J., and Schreyer, W., 1987, Phengite geobarometry based on the limiting assemblage with K-feldspar, phlogopite, and quartz: Contributions to Mineralogy and Petrology, v. 96, p. 212–224, https://doi.org/10.1007/BF00375235.

Menant, A., Angiboust, S., Monié, P., Oncken, O., and Guigner, J.-M., 2018, Brittle deformation during Alpine basal accretion and the origin of seismicity nests above the subduction interface: Earth and Planetary Science Letters, v. 487, p. 84–93, https://doi.org/10.1016/j.epsl.2018.01.029.

Mohn, G., Manatschal, G., Masini, E., and Müntener, O., 2011, Rift-related inheritance in orogens: A case study from the Austroalpine nappes in Central Alps (SE-Switzerland and N-Italy) [Geol Rundsch]: International Journal of Earth Sciences, v. 100, p. 937–961, https://doi.org/10.1007/s00531-010-0630-2.

Monjoie, P., Bussy, F., Schaltegger, U., Mulch, A., Lapierre, H., and Pfeifer, H.-R., 2007, Contrasting magma types and timing of intrusion in the Permian layered mafic complex of Mont Collon (Western Alps, Valais, Switzerland): Evidence from U/Pb zircon and $^{40}Ar/^{39}Ar$ amphibole dating: Swiss Journal of Geosciences, v. 100, p. 125–135, https://doi.org/10.1007/s00015-007-1210-8.

Montrasio, A., 1973, Strutture a pillow nelle anfiboliti del M. Forno (Penninico medio-Alpi Retichi): Rendiconti Accademia Nazionale Lincei: Scienzia Fisica Matematica Naturali, v. 54, p. 114–123.

Montrasio, A., Trommsdorff, V., Hermann, J., Müntener, O., and Spillmann, P., 2005, Carta Geologica della Valmalenco: Supplement to Scheizerische Mineralogische und Petrographische Mitteilungen, v. 85, p. 1.

Müller, W., Dallmeyer, R.D., Neubauer, F., and Thöni, M., 1999, Deformation-induced resetting of Rb/Sr and $^{40}Ar/^{39}Ar$ mineral systems in a low-grade, polymetamorphic terrane (Eastern Alps, Austria): Journal of the Geological Society of London, v. 156, p. 261–278, https://doi.org/10.1144/gsjgs.156.2.0261.

Müller, W., Mancktelow, N.S., and Meier, M., 2000, Rb-Sr microchrons of synkinematic mica in mylonites: An example from the DAV fault of the Eastern Alps: Earth and Planetary Science Letters, v. 180, p. 385–397, https://doi.org/10.1016/S0012-821X(00)00167-9.

Müntener, O., Hermann, J., Villa, I.M., and Trommsdorff, V., 1997, From Jurassic rifting to Cretaceous nappe formation: A combined $^{39}Ar/^{40}Ar$ and microprobe study on amphiboles: TERRA Abstracts, v. 1, p. 489.

Müntener, O., Hermann, J., and Trommsdorff, V., 2000, Cooling History and Exhumation of Lower-Crustal Granulite and Upper Mantle (Malenco, Eastern Central Alps): Journal of Petrology, v. 41, p. 175–200, https://doi.org/10.1093/petrology/41.2.175.

Müntener, O., Manatschal, G., Desmurs, L., and Pettke, T., 2010, Plagioclase peridotites in ocean-continent transitions: Refertilized mantle domains generated by melt stagnation in the shallow mantle lithosphere: Journal of Petrology, v. 51, p. 255–294, https://doi.org/10.1093/petrology/egp087.

Obara, K., and Kato, A., 2016, Connecting slow earthquakes to huge earthquakes: Science, v. 353, p. 253–257, https://doi.org/10.1126/science.aaf1512.

Oleskevich, D.A., Hyndman, R.D., and Wang, K., 1999, The updip and downdip limits to great subduction earthquakes: Thermal and structural models of Cascadia, south Alaska, SW Japan, and Chile: Journal of Geophysical Research. Solid Earth, v. 104, p. 14,965–14,991, https://doi.org/10.1029/1999JB900060.

Peretti, A., 1985, Der Monte-del-Forno-Komplex am Bergell-Ostrand: Seine Lithostratigraphie, alpine Tektonik und Metamorphose: Eclogae Geologicae Helvetiae, v. 78, p. 23–48.

Picazo, S.M., Ewing, T.A., and Müntener, O., 2019, Paleocene metamorphism along the Pennine-Austroalpine suture constrained by U-Pb dating of titanite and rutile (Malenco, Alps): Swiss Journal of Geosciences, p. 1–26, https://doi.org/10.1007/s00015-019-00346-1.

Platt, J.P., 1986, Dynamics of orogenic wedges and the uplift of high-pressure metamorphic rocks: Geological Society of America Bulletin, v. 97, p. 1037–1053, https://doi.org/10.1130/0016-7606(1986)97<1037:DOOWAT>2.0.CO;2.

Polino, R., Dal Piaz, G.V., and Gosso, G., 1990, Tectonic erosion at the Adria margin and accretionary processes for the Cretaceous orogeny of the Alps: Mémoires de la Société Géologique de France, v. 156, p. 345–367.

Price, J.B., Wernicke, B.P., Cosca, M.A., and Farley, K.A., 2018, Thermochronometry across the Austroalpine-Pennine Boundary, Central Alps, Switzerland: Orogen-perpendicular normal fault slip on a major "overthrust" and its implications for orogenesis: Tectonics, v. 37, p. 724–757, https://doi.org/10.1002/2017TC004619.

Rageth, R., 1984, Intrusiva und Extrusiva der Bernina-Decke zwischen Morteratsch und Berninapass (Graubunden): Schweizerische Mineralogische und Petrographische Mitteilungen, v. 64, p. 83–109.

Ratschbacher, L., 1986, Kinematics of Austro-Alpine cover nappes: Changing translation path due to transpression: Tectonophysics, v. 125, p. 335–356, https://doi.org/10.1016/0040-1951(86)90170-8.

Ring, U., Ratschbacher, L., and Frisch, W., 1988, Plate-boundary kinematics in the Alps: Motion in the Arosa suture zone: Geology, v. 16, p. 696–698, https://doi.org/10.1130/0091-7613(1988)016<0696:PBKITA>2.3.CO;2.

Ring, U., Ratschbacher, L., Frisch, W., Biehler, D., and Kralik, M., 1989, Kinematics of the Alpine plate-margin: Structural

styles, strain and motion along the Penninic-Austroalpine boundary in the Swiss-Austrian Alps: Journal of the Geological Society of London, v. 146, p. 835–849, https://doi.org/10.1144/gsjgs.146.5.0835.

Rowe, C.D., Moore, J.C., and Remitti, F., 2013, The thickness of subduction plate boundary faults from the seafloor into the seismogenic zone: Geology, v. 41, p. 991–994, https://doi.org/10.1130/G34556.1.

Rubatto, D., Gebauer, D., and Compagnoni, R., 1999, Dating of eclogite-facies zircons: The age of Alpine metamorphism in the Sesia-Lanzo Zone (Western Alps): Earth and Planetary Science Letters, v. 167, p. 141–158, https://doi.org/10.1016/S0012-821X(99)00031-X.

Saffer, D.M., and Wallace, L.M., 2015, The frictional, hydrologic, metamorphic and thermal habitat of shallow slow earthquakes: Nature Geoscience, v. 8, p. 594–600, https://doi.org/10.1038/ngeo2490.

Scaillet, S., 1996, Excess ^{40}Ar transport scale and mechanism in high-pressure phengites: A case study from an eclogitized metabasite of the Dora-Maira nappe, western Alps: Geochimica et Cosmochimica Acta, v. 60, p. 1075–1090, https://doi.org/10.1016/0016-7037(95)00440-8.

Schmid, S.M., Fügenschuh, B., Kissling, E., and Schuster, R., 2004, Tectonic map and overall architecture of the Alpine orogen: Eclogae Geologicae Helvetiae, v. 97, p. 93–117, https://doi.org/10.1007/s00015-004-1113-x.

Schwarz, W.H., and Trieloff, M., 2007, Intercalibration of ^{40}Ar-^{39}Ar age standards NL-25, HB3gr hornblende, GA1550, SB-3, HD-B1 biotite and BMus/2 muscovite: Chemical Geology, v. 242, p. 218–231, https://doi.org/10.1016/j.chemgeo.2007.03.016.

Sherlock, S., and Kelley, S., 2002, Excess argon evolution in HP-LT rocks: A UVLAMP study of phengite and K-free minerals, NW Turkey: Chemical Geology, v. 182, p. 619–636, https://doi.org/10.1016/S0009-2541(01)00345-X.

Sibson, R.H., 2013, Stress switching in subduction forearcs: Implications for overpressure containment and strength cycling on megathrusts: Tectonophysics, v. 600, p. 142–152, https://doi.org/10.1016/j.tecto.2013.02.035.

Spillmann, P., 1993, Die Geologie des penninisch-ostalpinen Grenzbereichs im südlichen Berninagebirge [Ph.D. thesis]: Zürich, ETH Zürich, 262 p.

Spillmann, P., and Büchi, H.J., 1993, The Pre-Alpine Basement of the Lower Austro-Alpine Nappes in the Bernina Massif (Grisons, Switzerland; Valtellina, Italy), *in* von Raumer, J.F., and Neubauer F., eds., The Pre-Mesozoic Geology in the Alps: Berlin-Heidelberg–New York–Tokyo, Springer, p. 457–467, https://doi.org/10.1007/978-3-642-84640-3_27.

Staub, R., 1946, Geologische Karte der Berninagruppe 1:50,000, Spez.-Karte Nr. 118: Scheiz. Geol. Kommission.

Stöckhert, B., 2002, Stress and Deformation in Subduction Zones: Insight from the Record of Exhumed Metamorphic Rocks: Geological Society of London, Special Publications, v. 200, p. 255–274, https://doi.org/10.1144/GSL.SP.2001.200.01.15.

Trommsdorff, V., 1983, Metamorphose magnesiumreicher Gesteine: Kritischer Vergleich von Natur, Experiments und thermodynamischer Datenbasis: Fortschritte der Mineralogie, v. 61, p. 283–308.

Trommsdorff, V., and Evans, B.W., 1977, Antigorite-ophicarbonates: Contact metamorphism in Valmalenco, Italy: Contributions to Mineralogy and Petrology, v. 62, p. 301–312, https://doi.org/10.1007/BF00371017.

Trommsdorff, V., Piccardo, G.B., and Montrasio, A., 1993, From magmatism through metamorphism to sea floor emplacement of subcontinental Adria lithosphere during pre-Alpine rifting: Schweizerische Mineralogische und Petrographische Mitteilungen, v. 73, p. 191–204.

Trommsdorff, V., Montrasio, A., Hermann, J., Müntener, O., Spillmann, P., and Gieré, R., 2005, The Geological Map of Valmalenco: Schweizerische Mineralogische und Petrographische Mitteilungen, v. 85, p. 1–13, https://doi.org/10.1542/peds.2009-2791.

Trümpy, R., 1975, Penninic-Austroalpine Boundary in the Swiss Alps: A presumed Former Continental Margin and its Problems: American Journal of Science, v. 275-A, p. 209–238.

Ulrich, T., and Borsien, G.R., 1996, Fedozer Metagabbro und Forno-Metabasalt (Val Malenco, Norditalien): Vergleichende Petrographische und Geochemische Untersuchungen: Schweizerische Mineralogische und Petrographische Mitteilungen, v. 76, p. 521–535.

Uto, K., Ishizuka, O., Matsumoto, A., Kamioka, H., Togashi, S., and Togashi, S., 1997, Laser-heating ^{40}Ar/^{39}Ar dating system of the Geological Survey of Japan: System outline and preliminary results: Bulletin of the Geological Survey of Japan, v. 48, p. 23–46.

Vannucchi, P., Remitti, F., and Bettelli, G., 2008, Geological record of fluid flow and seismogenesis along an erosive subducting plate boundary: Nature Letters, v. 451, p. 699–703, https://doi.org/10.1038/nature06486.

Villa, I.M., 1998, Isotopic closure: Terra Nova, v. 10, p. 42–47, https://doi.org/10.1046/j.1365-3121.1998.00156.x.

Villa, I.M., Hermann, J., Müntener, O., and Trommsdorff, V., 2000, ^{39}Ar-^{40}Ar dating of multiply zoned amphibole generations (Malenco, Italian Alps): Contributions to Mineralogy and Petrology, v. 140, p. 363–381, https://doi.org/10.1007/s004100000197.

Villa, I.M., De Bièvre, P., Holden, N.E., and Renne, P.R., 2015, IUPAC-IUGS recommendation on the half life of ^{87}Rb: Geochimica et Cosmochimica Acta, v. 164, p. 382–385, https://doi.org/10.1016/j.gca.2015.05.025.

Webber, S., Ellis, S., and Fagereng, Å., 2018, Virtual shear box experiments of stress and slip cycling within a subduction interface mélange: Earth and Planetary Science Letters, v. 488, p. 27–35, https://doi.org/10.1016/j.epsl.2018.01.035.

Whitney, D.L., and Evans, B.W., 2010, Abbreviations for names of rock-forming minerals: The American Mineralogist, v. 95, p. 185–187, https://doi.org/10.2138/am.2010.3371.

Wiederkehr, M., Sudo, M., Bousquet, R., Berger, A., and Schmid, S.M., 2009, Alpine orogenic evolution from subduction to collisional thermal overprint: The ^{40}Ar/^{39}Ar age constraints from the Valaisan Ocean, central Alps: Tectonics, v. 28, https://doi.org/10.1029/2009TC002496.

Wilke, F.D., O'Brien, P.J., Gerdes, A., Timmerman, M.J., Sudo, M., and Khan, M.A., 2010, The multistage exhumation history of the Kaghan Valley UHP series, NW Himalaya, Pakistan from U-Pb and ^{40}Ar/^{39}Ar ages: European Journal of Mineralogy, v. 22, p. 703–719, https://doi.org/10.1127/0935-1221/2010/0022-2051.

Yamaguchi, A., Ishikawa, T., Kato, Y., Nozaki, T., Meneghini, F., Rowe, C.D., Moore, J.C., Tsutsumi, A., and Kimura, G., 2014, Fluid-rock interaction recorded in black fault rocks in the Kodiak accretionary complex, Alaska: Earth, Planets, and Space, v. 66, p. 58, https://doi.org/10.1186/1880-5981-66-58.